

# Taphonomy of microorganisms and microbial microtextures at sulfidic hydrothermal vents: A case study from the Roman Ruins black smokers, Eastern Manus Basin

Raphael J. Baumgartner<sup>1,2</sup> | Siyu Hu<sup>1</sup> | Martin J. Van Kranendonk<sup>2</sup> | Michael Verrall<sup>1</sup>

<sup>1</sup>CSIRO Mineral Resources, Australian Resources Research Centre, Kensington, Western Australia, Australia

<sup>2</sup>Australian Centre for Astrobiology, and School of Biological, Earth and Environmental Sciences, The University of New South Wales, Kensington, New South Wales, Australia

## Correspondence

Raphael J. Baumgartner, CSIRO Mineral Resources, Australian Resources Research Centre, Kensington, WA, Australia.  
Email: [raphael.baumgartner@csiro.au](mailto:raphael.baumgartner@csiro.au)

## Abstract

Biological activity at deep-sea hydrothermal chimneys is driven by chemotrophic microorganisms that metabolize chemicals from the venting high-temperature fluids. Understanding taphonomy and microbial microtextures in such environments is a necessity for micropaleontological and palaeoecological research. This study examines fossilized microorganisms and related microtextures in a recent black smoker from the Roman Ruins hydrothermal vent site, Eastern Manus Basin offshore of Papua New Guinea. Whereas the center of the examined sulfide chimney is dominated by high-temperature mineralogy (chalcopyrite and dendritic sphalerite), filamentous and coccoidal biomorphs occur in an outer, warm zone of mixing between hydrothermal fluids and seawater, which is indicated by their occurrence within colloform and botryoidal pyrite of barite–pyrite coprecipitates. Both morphotypes can be interpreted as thermophilic microorganisms based on their occurrence in a high-temperature habitat. Their separate (non-commensal) occurrence hints at sensitivities to microenvironmental conditions, which is expectable for strong temperature, pH, and redox gradients at the walls of deep-sea hydrothermal chimneys. Whereas both morphotypes experienced mild thermal overprint, taphonomic differences exist: (i) spaces left by cells in filamentous fossils are predominately filled by silica, whereas inter/extracellular features (crosswalls/septae and outer sheaths) are pyritized; (ii) coccoidal fossils show both silica- and pyrite-infilled interiors, and generally better preservation of cell walls. These different manifestations presumably relate to an interplay between microenvironmental and biological factors, potentially contrasting metabolisms, and differences in cell wall chemistries of distinct bacteria and/or archaea. A further hypothesis is that the coccoidal features represent biofilm-forming organisms, whose organic matter derivatives contributed to the formation of intimately associated wavy and wrinkly carbonaceous laminations that are at least locally distinguishable from the texture of the surrounding pyrite. Hence, the presented data provide evidence that microtextures of microbiota from hydrothermal systems can have a similar significance for palaeobiological research as those from sedimentary environments.

This is an open access article under the terms of the [Creative Commons Attribution-NonCommercial](https://creativecommons.org/licenses/by-nc/4.0/) License, which permits use, distribution and reproduction in any medium, provided the original work is properly cited and is not used for commercial purposes.

© 2022 The Authors. *Geobiology* published by John Wiley & Sons Ltd.

## KEYWORDS

hydrothermal vent, microbial microtexture, micro-organism, sulfide, taphonomy

## 1 | INTRODUCTION

Deep-sea hydrothermal vents—regions on the seafloor where hot hydrothermal fluids are expelled into cold seawater—are areas of high biological productivity fueled by chemotrophic microorganisms, and considered as potential analog sites for the origin of life on Earth (e.g. Jannash & Mottl, 1985; Lutz, 1993; Martin et al., 2008; McCollom & Shock, 1997; Mullineaux et al., 2018; Nakagawa & Takai, 2008; Zirenberg et al., 2000). Despite their remote locations, there has been a steep increase in knowledge about these ecosystems, especially concerning habitat heterogeneity and biodiversity. Detailed information now exists about the interactions between microbes and their dynamic fluid environment, and the physiologies and metabolisms of microspecies, which can be deduced from genomic or biomarker analyses (e.g. Huber et al., 2007; McCollom & Schock, 1997; Nakagawa et al., 2005; Nercessian et al., 2005; Reysenbach et al., 2020; Skennerton et al., 2015; Takai & Hirokoshi, 1999; Xie et al., 2011). Insights into these microbe–mineral systems can also be gained from fossil microorganisms and microbially induced mineral textures. Of particular interest are organisms flourishing closest to hydrothermal venting, especially the walls of sulfide chimneys, because they can aid in approximating the general boundaries of microbial habitability (Merino et al., 2019; among others). Moreover, understanding taphonomic processes, and the general biogenicity of microfossils and mineral structures in such systems, is a necessity for interpreting traces of life preserved in the geological record (e.g. Georgieva et al., 2018; Li & Kusky, 2001; Rasmussen, 2000; Wacey et al., 2013, 2014).

Silification is perhaps the most important and best understood process for preservation, regardless of whether it occurs in terrestrial environments or in the oceans (Al-Hanbali et al., 2001; Bower et al., 2017; Jones & Renaut, 2003; Konhauser et al., 2005; Orange et al., 2009; Reeves et al., 2014; Westall et al., 1995). Preservation via pyritization has been studied for both macrofauna (e.g. Briggs et al., 1991; Le Bris et al., 2008; Little & Herrington, 1999) and microscopic life colonizing sedimentary and hydrothermal realms. The studies of Georgieva et al. (2015) and Georgieva et al. (2018), which report on the pyritization of recent and Silurian macrofauna from deep-sea vents, also document at high resolution the presence of intimately associated, ubiquitously pyritized microorganisms. A range of pyritized biomorphs within phosphorite crusts from recent shelf deposits were reported in Cosmidis et al. (2013). The study of Schieber and Riciputi (2005) investigated filamentous biomorphs associated with iron sulfides in Ordovician sedimentary strata from the Winnipeg Formation, Canada. Concerning the more ancient rock record, Li and Kusky (2001) investigated biomorphs within sulfide mounds of 1.43 Ga fossil black smokers from northern China, but this occurrence requires re-examination at high resolution to

confirm their biogenicity. The studies of Wacey et al. (2013) and Javaux and Lepot (2018) characterized pyritized tubular sheaths of filamentous biomorphs from the ~1.9 Ga Gunflint chert (Northern America); Schopf et al. (2015) reported on pyrite encrusted deep-water biomorphs from the ~2.3 Ga Turee Creek Group (Western Australia); and Rasmussen (2000) as well as Wacey et al. (2014) examined the putative remains of black smoker microbiota in cherts from the 3.24 Ga Sulphur Springs Group (Western Australia). Lastly, Baumgartner et al. (2019) interpreted the strongly pyritized stromatolites in hydrothermal-sedimentary strata from the 3.48 Ga Dresser Formation (Australia) as biological based on their morphology and texture, micromineralogy, chemistry, and the presence of coherent strands and filaments composed of thermally mature organic matter, which were interpreted as the degraded remains of microbial communities.

From the above, it is evident that pyritization is an important process leading to the fossilization and preservation of ancient microbial features, but research focusing on more recent analogs remained scarce. Hence, to further understand microbial taphonomy and microbially mediated sulfide mineral textures in hydrothermally influenced environments, this study reports on the pyritization plus silification of different morphotypes of putative microbes that colonized the outer walls of a sulfidic chimney from the recent Roman Ruins hydrothermal vent site, Eastern Manus Basin. The covariation of vent mineralogy and microbial features provides information about the ambient parameters and processes that supported microbial growth. The fine-scale characterization of biomorphs within pyrite sheds light on the processes leading to preservation and how taphonomic differences may have been influenced by both ambient and microbial parameters and processes. Because one of the observed morphotypes appears to represent biofilm-forming organisms, it is also discussed how pyritized biofilm features may be discriminated from abiotic pyrite textures.

## 2 | SAMPLING LOCATION AND MATERIALS

The studied black smoker (CSIRO ID: 4134253A) was collected in 1993 from the Roman Ruins hydrothermal vent site, which is part of the PACMANUS (Papua New Guinea-Australia-Canada-Manus Basin) hydrothermal vent field in the Eastern Manus Basin offshore of Papua New Guinea (Figure 1). This zone of intense seafloor hydrothermal activity developed in conjunction with volcanic activity along extensional rifts in a spreading back-arc system between the Australian and Pacific plates (Binns, 2014; Martinez & Taylor, 1996; Taylor, 1979; Thal et al., 2014). Specifically, the studied material is a subsample of a larger sulfidic chimney sample (56 × 22 × 15 cm

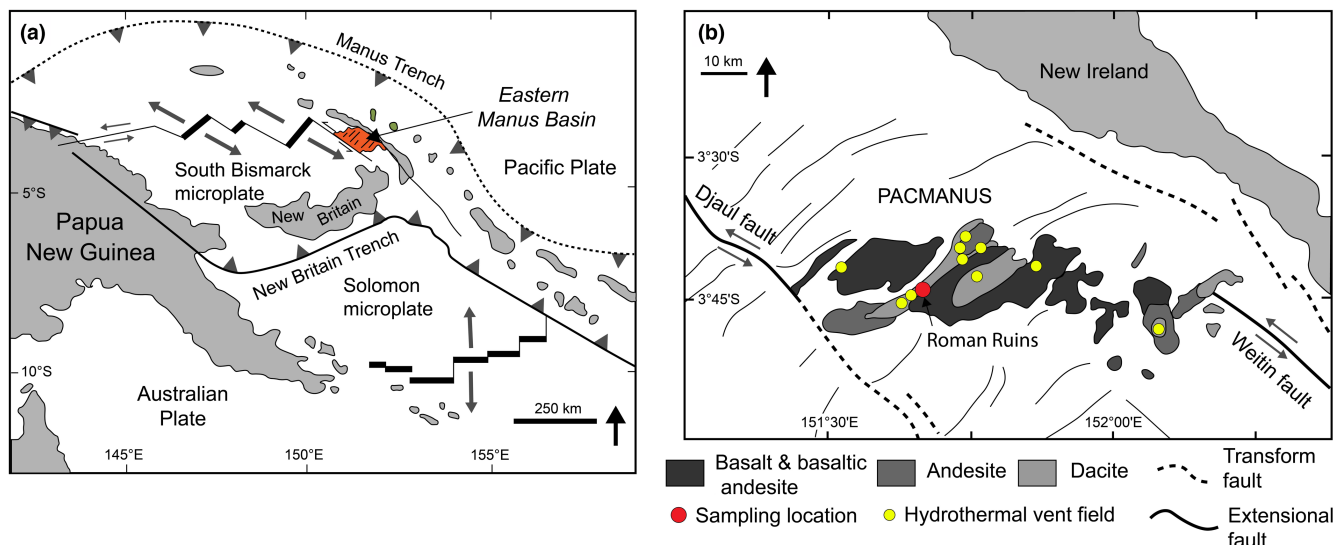


**FIGURE 1** Regional tectonic setting (a) and geology (b) of the Eastern Manus Basin. Major zones of hydrothermal activity, including the Roman Ruins Mills of the PACMANUS hydrothermal vent field, are indicated. Redrawn after Binns et al. (2002)

in size) that exhibits a Cu-rich interior and Zn-rich (sphalerite) outer zones that are coated by barite, sometimes with crusts of colloform and botryoidal pyrite (Binns et al., 2002). This switch from Cu- to Zn-dominated mineralogy is common in deep-sea sulfidic vents and reflects thermochemical gradients from the inner, hot zones of hydrothermal fluid orifices to outer, cooler zones that are commonly strongly affected by cooler seawater (Tivey, 2007).

### 3 | METHODS

Since its collection in 1993, the black smoker material examined in this study was preserved under cool and dry storage conditions. Thin sections, prepared from a fragment of sphalerite dendrites plus outer barite  $\pm$  pyrite crusts, were characterized using synchrotron radiation X-ray fluorescence microscopy (SR-XFM), optical microscopy, Raman spectroscopy, as well as scanning electron microscopy (SEM) imaging and energy dispersive X-ray spectroscopy (EDS) analyses. All but SR-XFM analyses were performed both prior to and after etching with concentrated nitric acid (70%  $\text{HNO}_3$ ), that is,  $\sim 60$  s exposure time, followed by quenching with distilled water and air drying ( $\sim 40^\circ\text{C}$ ) in a laboratory oven. Overall, nitric acid etching strongly corrodes pyrite, and thus exposes carbonaceous matter and comparatively corrosion-resistant constituent mineralogy, such as opaline silica, barite, and sphalerite.

Element maps of the banded to finely laminated pyrite and the surrounding mineralogy were acquired by SR-XFM at the Australian Synchrotron (Melbourne, Australia), which allows for rapid, semi-quantitative elemental mapping of large areas at high resolution ( $2\ \mu\text{m}^2$ ). The XFM beamline, which is equipped with a Maia 384 large-angle detector array and a Kirkpatrick-Baez (KB) mirror end station, provides a 4–20 keV monochromatic electron beam with a spot size

of  $2\ \mu\text{m}$  (Paterson et al., 2011). For this study, spectral data were acquired using count rates of 4–10 M/s and 0.3–0.4 keV energy resolution, and calibrated against analyses of Fe, Mn, Pt, and  $\text{YF}_3$  standard foils. Data processing was done in the program GeoPIXE, by standardless correction of the raw data and using the dynamic analysis methods described in Ryan, Kirkham, et al. (2010), Ryan, Siddons, et al. (2010).

Textures and mineral assemblages were first examined using a Zeiss 105 Axio Imager.A2 microscope at CSIRO Mineral Resources, Kensington (Perth). Backscattered electron (BSE) and secondary electron (SE) imagery, as well as elemental analysis and mapping by EDS, was carried out using an FEI XHR-Verios 460I field-emission SEM (FE-SEM) at Centre for Microscopy, Characterisation and Analysis (CMCA), University of Western Australia (UWA), and a Tescan Mira3 FEG-SE at CSIRO Mineral Resources, Kensington (Perth). On both machines, BSE and SE images were acquired using 5–10 keV acceleration voltage and 0.1–0.2 nA beam current, whereas EDS spot analysis and elemental mapping, which was done in Oxford Instruments' Aztec software, involved 10–15 kV acceleration voltage and 0.4 nA beam current. The electron images and EDS analyses were acquired without the use of a conductive coating; charging by the electron beams was mitigated by application of copper tape near the regions of interest. Image processing and measuring was done using the open-source programs ImageJ and IrfanView.

Raman spectroscopy analysis was carried out using a Horiba LabRam HR Evolution instrument (CSIRO Energy, Kensington, Perth) and a Witec alpha 300RA+ Raman probe (CMCA, UWA). The Horiba instrument is equipped with a multichannel air-cooled ( $\sim 70^\circ\text{C}$ ) Synapse Visible detector, and a 100 mW continuous wave (532 nm) diode laser from Laser Quantum. The Witec probe is combined with a peltier-cooled ( $\sim 60^\circ\text{C}$ ) Andor Newton CCD, and a Witec 532 nm laser source. On both instruments, 100 $\times$  objectives were

used for laser focusing to  $\sim 0.72\ \mu\text{m}$  beamwidth. Filtering decreased the laser powers to  $c. \leq 0.5\ \text{mW}$ . Spot analyses were conducted both using the Witec and Horiba instruments; spectra were collected with 600 grooves/mm in the  $\sim 200\text{--}2000\ \text{cm}^{-1}$  region, using 1 s exposure time and 100–300 accumulations. Maps were acquired using the Witec instrument at  $\sim 2.5\ \mu\text{m}$  resolution; individual spectra were collected with 600 grooves/mm in the  $200\text{--}2000\ \text{cm}^{-1}$  region using 3 s exposure time. The spectra were calibrated against the peaks of a Si wafer. Baseline correction, which was done in the software MagicPlot, involved baseline fitting through spectral intervals containing background only.

## 4 | RESULTS

### 4.1 | Textures, petrography, and mineralogy

In the studied chimney subsample, two main precipitation intervals are discernible. Both grade from (i) millimeter- to centimeter-scale columns of dendritic sphalerite, to (ii) irregular barite-pyrite ( $\pm$ opaline silica) precipitates (Figure 2). The occasionally multiply branching sphalerite aggregates exhibit bulbous/botryoidal outlines (Figure 2c), which can be explained by the coalescence of smaller sphalerite globules (Hu et al., 2019). The centers of sphalerite dendrites occasionally contain opaline silica and aggregates of spheroidal, polycrystalline pyrite, which are up to  $\sim 30\ \mu\text{m}$  in diameter, and defined by a concentrically laminated and in part radial fibrous nanotexture (Figure 3). Raman spectroscopy analysis shows that the pyrite in the sphalerite dendrites is enriched in carbonaceous matter, which is distinguishable from the epoxy of the thin section by distinctive spectral features in the wavenumber range of  $1000\text{--}1700\ \text{cm}^{-1}$  (see Figure 4a and below for a more detailed description of the Raman spectral features).

In both precipitation intervals, the sphalerite dendrites are terminated by barite-pyrite ( $\pm$ opaline silica) mineralization (Figures 2b,c and 5a), for which the intimate intergrowth textures between barite and pyrite indicate a (near-) synchronous precipitation of both these phases. Raman spectroscopy analysis shows that the opaline silica associated with barite and pyrite is opal-CT (opal-cristobalite/tridymite), as is consistent with a broad peak at  $\sim 345\ \text{cm}^{-1}$ , and minor peaks at  $\sim 235\ \text{cm}^{-1}$  and  $480\ \text{cm}^{-1}$  (see Figure 4a, and compare with Curtis et al., 2019). The barite occurs as irregular to radial aggregates of euhedral to anhedral, prismatic, or tabular/bladed to acicular crystals that are up to several hundred microns in length (Figures 2b,c and 5a,b). In interval 1, these barite crystal agglomerations are overlain by continuous or discontinuous layers of colloform pyrite. Occasionally, these pyrite layers are sharply terminated by sphalerite dendrites of interval 2 (Figure 2b). In the absence of distinctive layering, as is particularly the case in interval 2, the pyrite is mainly represented by botryoidal aggregates (compare Figure 2b with Figure 2c).

Both the colloform and botryoidal pyrite are finely laminated and variably enriched in carbonaceous matter plus opaline silica (see Figures 5b-d and 6, as well as the Raman spectroscopy analyses

of carbonaceous matter in Figure 4). The common geometric component is concentric pyrite, which, like the pyrite in the center of sphalerite dendrites, exhibits a concentrically laminated and radial fibrous nanotexture (compare Figure 3b,c with Figure 5e,f). In cycles of repeating patterns, these concentric growth forms grade into, or are overlain by, corrugated laminae with fibrous texture, whose thicknesses range between  $<1\ \mu\text{m}$  and up to several microns (Figure 5g). However, in some areas that contain intercalating laminae of carbonaceous matter plus opaline silica, as appear as dark gray color in BSE images (Figure 5c,h, and see the Raman spectroscopy data in Figure 4), the rhythmically laminated texture of pyrite is interrupted by more heterogeneous, wavy to wrinkly features. Notable among such aggregates enriched in carbonaceous matter is the frequent occurrence of micro-columnar growth forms, up to  $\sim 20\ \mu\text{m}$  in size, which comprise finely spaced, upward-convex lamination (Figure 5h).

### 4.2 | Filamentous and coccoidal morphotypes

The pyrite of both intervals hosts variably pyritized and silicified biomorphs. A filamentous morphotype is particularly prominent in the pyrite of precipitation interval 1, but only rarely occurs in interval 2, whereas a coccoidal morphotype occurs in pyrite from both intervals.

The mostly segmented, straight to slightly bent, filamentous morphotype, usually  $<1\ \mu\text{m}$  in diameter and up to several microns in length, commonly occurs in groups of tens of filaments and only rarely as isolated entities. In the former case, the filaments are bundled, interlaced, or lie parallel to one another, and show no preferred orientation relative to the texture of the pyrite matrix (Figure 7a-c). The filaments have a normal diameter distribution ( $0.20\text{--}0.65\ \mu\text{m}$ ;  $\sim 0.45\ \mu\text{m}$  median; Figure DR1a). Their (segmented) interiors are mostly filled by silica, as seen in electron imagery and indicated by strong signals of Si in EDS analysis, whereas immediately adjacent microstructures resembling crosswalls/septae and outer sheaths of filamentous microbes are for the most part pyritized (Figure 8a-b; Fig. S2). In rarer instances, however, the interiors are partially or entirely filled by pyrite and occasionally lined by dark rims in BSE imagery, the latter which presumably consist of both carbonaceous matter and opaline silica (Figure 8a,b). Overall, these filamentous features show striking similarities to the approximately equal-sized, pyrite-encased, filamentous microorganisms in Georgieva et al. (2015, their Figure 4) and Georgia et al. (2018, their Figures 3 and 4), which were reported from the pyritized walls of worm tubes at recent and ancient, deep-sea hydrothermal vents.

Coccoidal features, which mostly occur away from the filamentous biomorphs, are particularly prominent in the areas of wavy and wrinkly laminated to micro-columnar growths of carbonaceous matter-rich pyrite, where they occur as loose or tightly packed clusters of spherical to ellipsoidal entities (Figures 5h and 7d-f). Overall, the coccoidal morphotype shows a right-skewed diameter distribution in the  $<0.35\text{--}1.8\ \mu\text{m}$  range (mode  $\sim 0.5\ \mu\text{m}$ ; Figure DR1b).

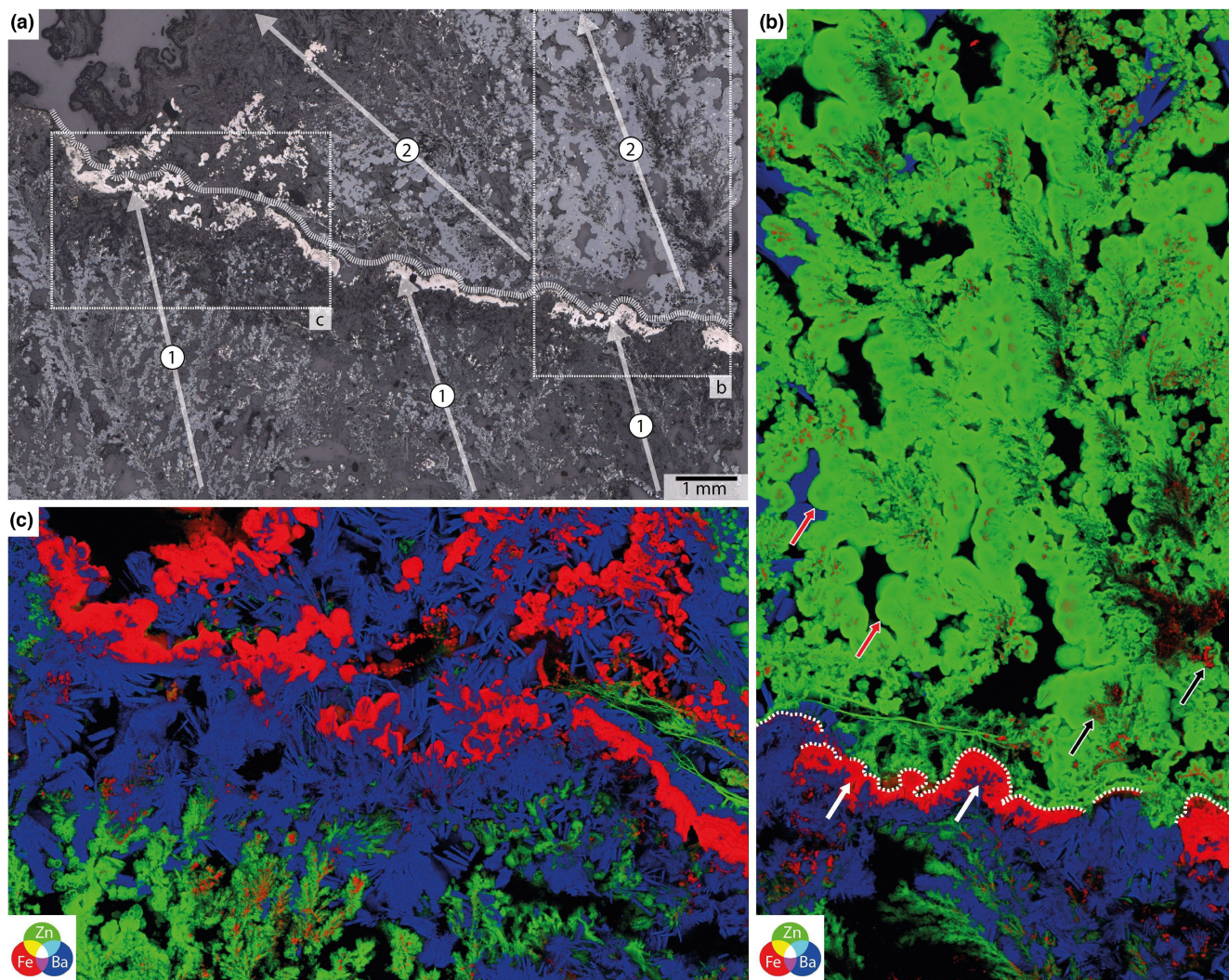


**FIGURE 2** Reflected light photomicrograph (a) and elemental distribution maps (b and c) of the studied sulfidic black smoker fragment. Note in (b and c) the close relationship between pyrite and barite, which are indicated by Fe and Ba, respectively. The barite is represented by coarse, radial aggregates of tabular crystals; compare with [Figure 5a,b](#). The numbered arrows and dashed line in (a) denote two separate precipitation intervals, each consisting of dendritic sphalerite mineralization that are terminated by barite–pyrite precipitates. The white arrows and lines in (b) indicate pyrite layers that are sharply terminated by dendritic sphalerite. The black arrows indicate pyrite (indicated by Fe) in the centers of sphalerite dendrites (compare with [Figure 3](#)). The red arrows indicate the bulbous/botryoidal outlines of sphalerite dendrites

Electron imaging combined with EDS elemental analysis ([Figures 7d-f](#) and [8c-d](#)) shows that the carbonaceous coccoidal forms are variably pyritized and silicified. Importantly, examples with pyrite infills and thin outlines composed of carbonaceous matter (plus opaline silica) are distinctly more common than among the filamentous microfossils (compare [Figure 7a-c](#) with [Figure 7d-f](#)).

Electron imaging of the filamentous biomorphs following nitric acid etching provides additional information about their microstructural characteristics, styles of preservation, as well as their spatial distributions and relationships with each other and the pyrite host ([Figure 9](#)). For example, it more clearly shows that these biomorphs show strongly silicified interiors ([Figure 9b-e](#)), and are oriented independently to pyrite textures, including filaments passing undisturbed across pyrite layering and circular pyrite aggregates ([Figure 9c-e](#)).

Raman spectroscopy analysis following nitric acid etching also reveals that, in rare instances, the areas around the filaments are not only pyritized and silicified but hematized ([Figures 4](#) and [9c](#)). The segmented interiors of the filaments are mostly pervasively silicified. No remnant outer sheaths, as would be expected for filamentous microbes wrapped in EPS, are observable, which is consistent with the strongly pyritized nature of microbes seen on unetched pyrite surfaces (compare [Figure 8a-b](#) with [Figure 9](#)). Moreover, as opposed to the coccoidal morphotype (see below), no coherent, wavy, and wrinkly laminae of carbonaceous matter occur in the vicinity of the filaments.

Nitric acid etching of pyrite also allows observation of several mineralization and preservation stages of the coccoidal biomorphs ([Figure 10](#)). The swarm of carbonaceous coccoidal biomorphs in

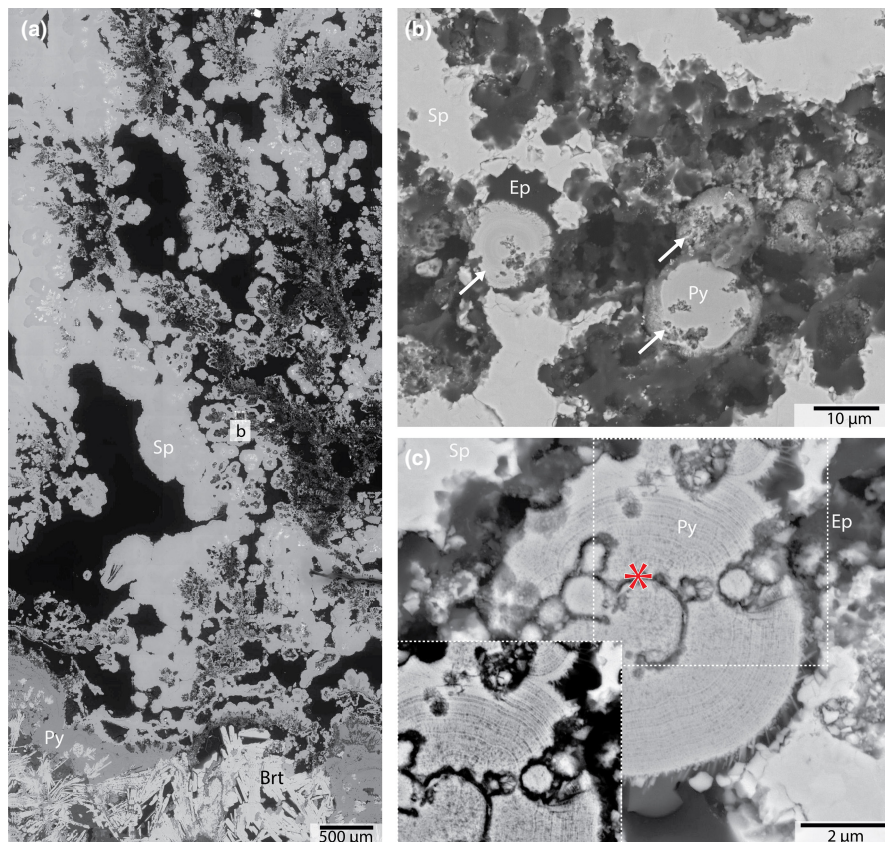


**FIGURE 3** Texture and mineralogy of the sphalerite dendrites. Note at the bottom of image (a) the presence of finely laminated pyrite in conjunction with irregular to radial aggregates of tabular barite crystals. The images (b) and (c) show spherulitic pyrite (white arrows) in the center of the sphalerite dendrites. The inset in (c) shows the nanoscale laminated and radial-fibrous interior of a pyrite spherulite. The dark gray materials in (b) and (c) is epoxy contaminant from thin section preparation. The asterisk in (c) indicates the location of Raman spectroscopy analysis (Figure 4). Brt = barite; Ep = epoxy; Op = opaline silica (opal-CT); Py = pyrite; Sp = sphalerite

Figure 10a-c, which often occurs in association with thick, wavy, and wrinkly laminae of carbonaceous matter plus opaline silica, comprises deformed carbonaceous matter spheres that are in part empty owing to acid dissolution of their originally pyritic interiors (Figure 7d-f). Other areas exhibit a wider range of carbonaceous coccoidal features, ranging from well-preserved, perfectly round, or oval, partially silicified entities, to circular cavities in pyrite, sometimes with rounded pyrite cores, which presumably represent the molds of vanished coccoids (Figures 8c,d and 10d-f). Well-preserved carbonaceous coccoidal biomorphs commonly occur in association with, and are draped by, smooth or ropey sheaths of carbonaceous matter, which occasionally establish matrices reminiscent of connective networks (Figure 10d-f; Fig. S3). Lastly, a large fraction of coccoidal entities, especially those with diameters of  $\geq 0.7\text{--}0.8\ \mu\text{m}$ , exhibit a pitted microtexture made of round to hexagonal pits, which lends them a golf ball-like appearance (Figures 8c and 10e-f).

### 4.3 | Raman spectroscopy of carbonaceous matter

Raman spectroscopy analysis of carbonaceous matter, acquired both prior to and after nitric acid etching on the biomorphs (filamentous and coccoidal) and carbonaceous matter layering in pyrite, resolves consistent spectral features in the  $1000\text{--}1700\ \text{cm}^{-1}$  range, with two distinctive maxima at  $\sim 1365\ \text{cm}^{-1}$  and  $\sim 1585\ \text{cm}^{-1}$  that are referred to as D and G band, respectively (Figure 4a). Generally, the widths and positions of both these bands, and hence their spectral

separation (distance D-G), are sensitive to the processes that occur during heating and carbonization, that is, the distance D-G increases with increasing thermal maturity, whereas the width of the G band decreases (Henry et al., 2019; among others). In this study, the D-G distance in spectra from both the biomorphs and carbonaceous matter layering in multiple areas across the sample falls into the  $217\text{--}222\ \text{cm}^{-1}$  range (Figure 4b). These low values, the generally large width of the G band [full width at half maximum (FWHM)  $\sim 155\ \text{cm}^{-1}$ ], and the general shape of the spectra in the  $1000\text{--}1700\ \text{cm}^{-1}$  range (Figure 4b), are consistent with organic matter that experienced only subtle heating and little thermal cracking ( $<100^\circ\text{C}$ , estimated; see Henry et al., 2019, their Figures 4 and 5).

## 5 | DISCUSSION

### 5.1 | Interpretation of filamentous and coccoidal biomorphs

This study reports the occurrence of variably pyritized and silicified carbonaceous microbiomorphs within colloform and botryoidal pyrite in the outer barite-sphalerite crust of a recent black smoker chimney. As discussed in the following, an interpretation of these features as in situ fossilized microorganisms is supported by their occurrence in a low-temperature context, their relative distributions, and particularly their morphological, microtextural, and compositional characteristics.

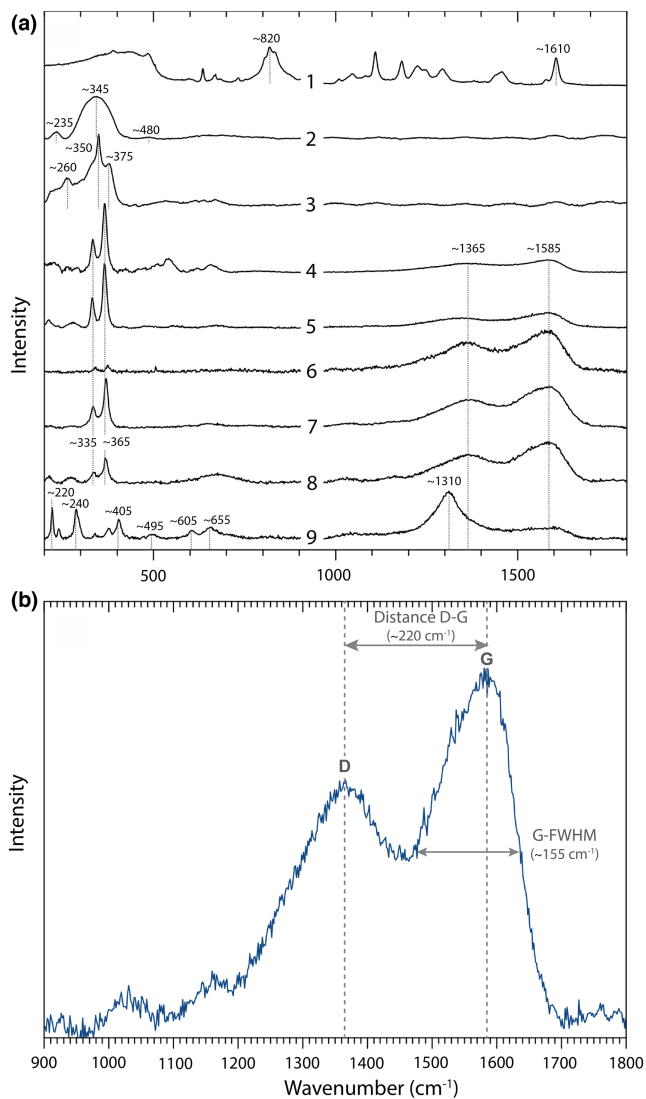


**FIGURE 4** Representative results from Raman spectroscopy analyses on major mineralogy and putative microbial features. a) Raman spectra of selected features: (1) glass slide and epoxy resin of thin section; (2) opaline silica in Figure 7b (opal-CT; see text); (3) sphalerite of sphalerite dendrites in Figure 3c; (4) spheroidal pyrite in the center of sphalerite dendrites in Figure 3c; (5 and 6) carbonaceous matter layering in colloform pyrite prior to and after nitric acid etching (Figures 5h and 10a); (7) filamentous morphotype in pyrite prior to nitric acid etching (Figure 7c); (8) coccoidal morphotype in pyrite following nitric acid etching (Figure 8c); (9) filamentous morphotype in pyrite (+hematite) following nitric acid etching (Figure 9c). The dashed lines indicate the major peaks in each spectrum. The diagnostic epoxy peaks in spectrum (1) at 820  $\text{cm}^{-1}$  and 1610  $\text{cm}^{-1}$  are used in large-area Raman spectroscopy mapping to discriminate bona fide carbonaceous matter from epoxy contaminants (Figure 6). The indicated peaks in spectrum (2) are consistent with microcrystalline opal (i.e., opal-CT; Curtis et al., 2019). In spectrum (3), the low wavenumber peak at ~350  $\text{cm}^{-1}$  relates to sphalerite of sphalerite dendrites, whereas the origins of peaks at 260 and 375  $\text{cm}^{-1}$  are uncertain. The low wavenumber peaks in spectra (4–8) relate to pyrite, and those in (9) to hematite; compare with Marshall et al. (2020). In spectra (4–9), the peaks at ~1365  $\text{cm}^{-1}$  and 1585  $\text{cm}^{-1}$  relate to carbonaceous matter. The peak at ~1310  $\text{cm}^{-1}$  in spectrum (9) relates to hematite. (b) Spectrum of carbonaceous matter in the 900–1800  $\text{cm}^{-1}$  range. Indicated are the parameters that allow for thermal maturity estimation (see main text), that is, full width at half maximum of the G band (FWHM), and spectral distance between the D and G bands (distance D-G)

Consistent with a biological interpretation, the filamentous features show a cell-like morphology and are enriched in carbonaceous matter (Figures 8a–b and 4). However, these observations alone are inconclusive, because filamentous biomorphic structures can also form abiotically (e.g., filamentous mineral aggregation), and carbonaceous substances like soluble bitumen can be transported from exogenous sources, especially under hydrothermal conditions. Besides these potential ambiguities, the filamentous structures commonly occur in restricted swarms that are reminiscent of microbial colonization, consistently show a narrow, normally distributed diameter (mean ~0.45  $\mu\text{m}$ ; Fig. S1b) that is consistent with the presence of a single microbe species, and exhibit well-preserved microtextures reminiscent of cellular features. The latter includes segmented interiors that are filled by opaline silica, and microtextures that are consistent with pyritized cell walls and septae (Figures 7a–c and 8a–b). A biogenic interpretation of the filamentous structures is also supported by their remarkably close resemblance to the approximately equal-sized, pyrite-encased filamentous microfossils from deep-sea hydrothermal vents reported in Georgieva et al. (2015, their Figure 4).

The identification of coccoidal microfossils in geological samples is notoriously difficult. Even for well-preserved materials, it can be impossible to unambiguously distinguish simple shaped coccoidal microorganisms from abiotic mimics, such as orbicular and botryoidal opaline silica (e.g., Lepot, 2020), and carbonaceous spheres that can form by Ostwald ripening or non-templated self-assembly (Nims et al., 2021). Nonetheless, multiple lines of evidence lend support for the biogenicity of the coccoidal forms studied here. Firstly, they are distributed unevenly, mostly away from the filamentous microfossils, in swarms that are reminiscent of microbial colonization (Figure 7d–f). Frequency diameter distributions of the coccoids are right skewed, with a mode that is distinctly above the lower limit of prokaryotic organisms (i.e., ~0.5  $\mu\text{m}$ , compared to ~0.25  $\mu\text{m}$  described in Luef et al., 2015), and falls within the range of cell diameters known from coccoidal species at deep-sea hydrothermal vents (e.g., *Methanococcus jannaschii*; Park & Clark, 2002). The observed spread of diameters (<0.35–1.8  $\mu\text{m}$ ; Figure DR1b) can be attributed to the presence of one or more species, for which original cell size variations—such as relating to asexual reproduction and cell growth, or regulation of cell size in response to microenvironmental conditions and nutrient availability—were perhaps further altered by contraction during fossilization (see discussion below).

The coccoidal forms also show internal and external microfeatures that are consistent with fossilized microorganisms. Electron imaging resolves thin walls that resemble cell membranes, and cores of pyrite or quartz that can be interpreted as post-mortem infills (Figure 7d–f). Consistent with the birth and death of labile cells in a dynamic fluid environment, the coccoidal features also show

distinctive preservational differences, that is, perfectly spheroidal carbonaceous microstructures can occur side-by-side with variably deformed/pitted coccoids and the outer molds of vanished entities (Figures 8c-d and 10d-f). Lastly, many swarms of coccoidal biomorphs contain smooth or ropey sheaths of carbonaceous matter (Figure 10e and DR3), which can wrap around the coccoids and establish matrices reminiscent of connective networks (Figure 10d-e and DR3). These features are interpreted as being of biological origin because of their striking microtextural resemblance to extracellular polymeric substance (EPS) secreted by biofilm-forming organisms. Whereas alternative origins from migrated hydrocarbons (bitumens) cannot be discounted entirely, a production of vast quantities of EPS, which is deemed to play a key role in biofilm wrinkling (e.g., Westall et al., 2000), also holds as an explanation for the intimate relationships between swarms of coccoidal features and the wavy/wrinkly carbonaceous matter layering within the colloform and botryoidal pyrite precipitates (see further discussion below and Figures 5h, 10a-b and 11).

## 5.2 | Microbial activity and microhabitat heterogeneity

The above discussion provides evidence for filamentous and coccoidal microorganisms populating the outer barite- and pyrite-rich crusts of a deep-sea black smoker chimney. Indeed, it is well established that deep-sea sulfidic venting systems can support diverse benthic communities fueled by chemotrophic microorganisms, which fix inorganic carbon (typically C of CO<sub>2</sub>) through energy derived from the oxidation of hydrothermally sourced compounds, especially H<sub>2</sub>, H<sub>2</sub>S, CH<sub>4</sub>, or reduced Fe and Mn (e.g. Jannash & Mottl, 1985; Lutz, 1993; Martin et al., 2008; McCollom & Shock, 1997; Mullineaux et al., 2018; Nakagawa & Takai, 2008; Zirenberg et al., 2000). This inference holds true for the hydrothermal vent fields from the Eastern Manus Basin of Papua New Guinea, from which microbial communities including chemoautotrophic and chemoheterotrophic microorganisms dependent on sulfur, nitrogen, or hydrogen metabolisms have been reported (e.g. Kimura et al., 2003; Meier et al., 2019; Takai et al., 2001; Wang et al., 2017).

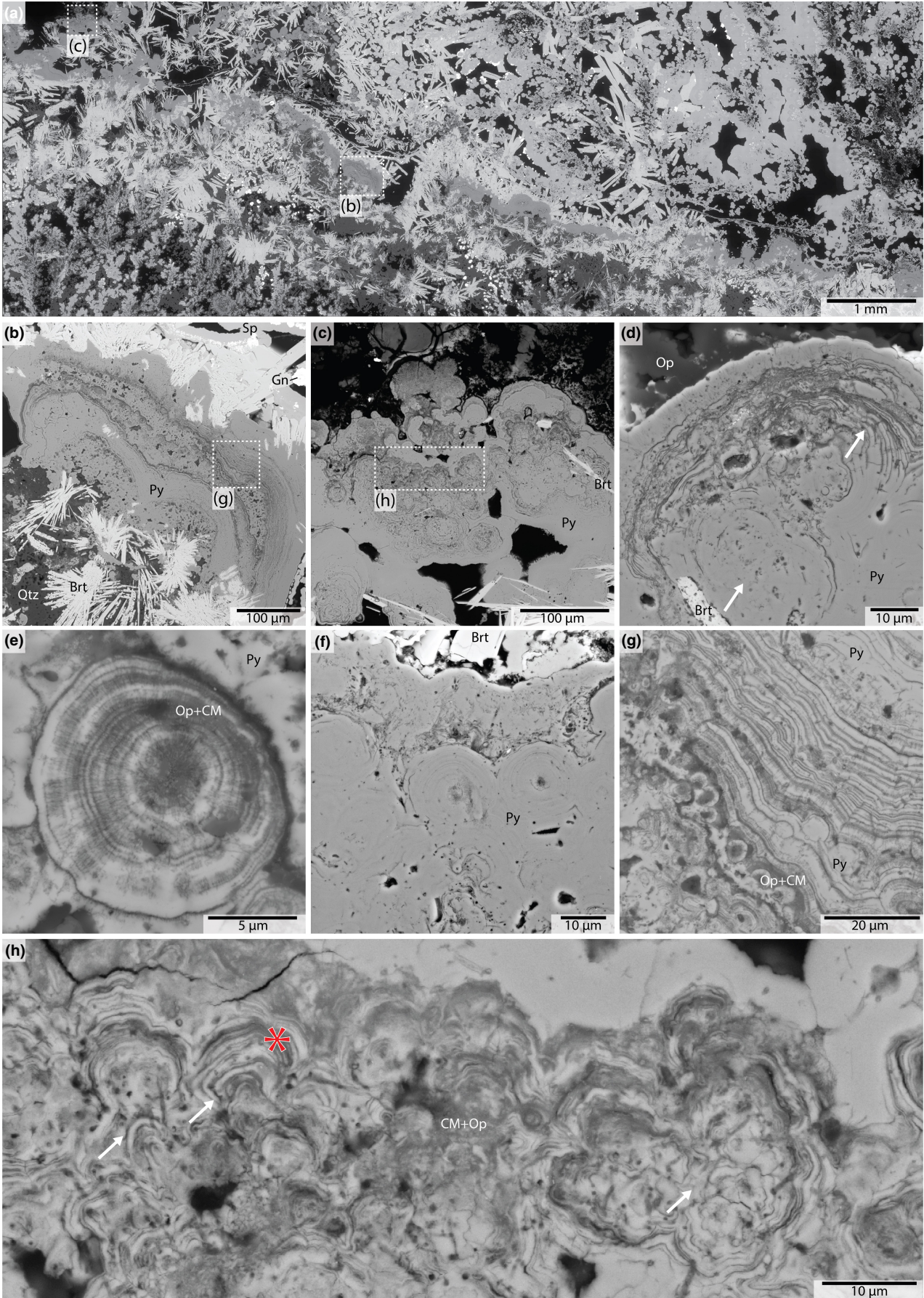
Specifically, active hydrothermal vents can harbor diverse communities of thermophilic chemoautotrophs and chemoheterotrophs, that is, microorganisms that thrive in the temperature range of ~40–120°C (Kashefi & Lovley, 2003; Takai et al., 2008). With respect to

the black smoker sample studied here, the transitions from sphalerite dendrites to barite-pyrite precipitates—indicated in Figures 2 and 11—could represent spatially constrained habitats for such heat-loving chemotrophic microbes. Up to ~350°C was recorded for the venting fluids from the Roman Ruins hydrothermal field (Reeves et al., 2011). Here, cooling to lower temperatures at the outer zones of vent chimneys is signaled by the presence of abundant barite (Figure 2), that is, its abrupt occurrence, tabular habit, and irregular to radial aggregation pattern is diagnostic for precipitation during mixing between hot hydrothermal fluids and cold, sulfate-rich seawater (Griffith & Paytan, 2012; Jamieson et al., 2016).

For the analyzed sample, fluid cooling to temperatures permitting life aligns with the spatially constrained occurrence of the microbial features, that is, filamentous and coccoidal microfossils, are absent in the higher-temperature dendritic sphalerite mineralization, but abundant in the areas of lower-temperature barite-pyrite co-precipitation (Figure 5). This observation supports the formation of the sphalerite dendrites at temperature conditions that prohibited life, which is also indicated by their bulbous/botryoidal habit and micromineralogical traits that point to rapid precipitation at elevated temperature (>120°C) and supersaturated conditions (Hu et al., 2019). Whereas the central portions of sphalerite dendrites comprise concentrically laminated, spherulitic pyrite plus carbonaceous matter (Figure 3), the latter was presumably recycled over short distance from the microbial features in the nearby colloform and botryoidal pyrite mineralization, and thus unlikely originated from now vanished (degraded) microorganisms flourishing during an early stage of sphalerite precipitation.

The exquisite preservation of filamentous and coccoidal microfossils also allows discussing whether their properties and relationships to one another and the host mineralogy (Figures 5-10) provide information about the nature of the microbes. The hypothesis that the fossils represent thermophilic prokaryotes (archaea or bacteria) is supported by their small cell volumes and general occurrence in a high-temperature habitat in vicinity to expulsions of hot hydrothermal fluids. Commensal/symbiotic relationships between the observed microbe types are unlikely given their predominately separate occurrence. This, and the seemingly low species diversity, may reflect sensitivities to the strong physicochemical gradients that can occur at the walls of deep-sea hydrothermal chimneys. As discussed in more detail below, it is plausible that the coccoidal microfossils represent biofilm-forming organisms, which is indicated by their association with carbonaceous microstructures reminiscent

**FIGURE 5** Macro- and microtextural characteristics of colloform and botryoidal pyrite. (a) Backscattered electron (BSE) image of barite-pyrite precipitates and relating mineralogy: bright white = Pb- and As-rich mineral grains; white = barite; light gray = sphalerite; medium gray = pyrite; dark gray = opaline silica; black = resin of the thin section. (b-d) Microtextural variations within colloform pyrite (b) and botryoidal pyrite (c and d). The left arrow in (d) indicates interleaving, concentric pyrite aggregates, whereas the right arrow indicates overgrowths of corrugated to wavy and wrinkly laminae. (e-g) Multilayered, radial-fibrous, concentric pyrite aggregates in colloform pyrite. The dark gray material is carbonaceous matter plus opaline silica. (h) Microtextural variations in botryoidal pyrite. The left arrows indicate micro-columnar structures with upward-convex lamination. The right arrow indicates multiply lobed, finely layered pyrite aggregates. The black, rounded pores throughout the pyrite are mostly coccoidal morphotypes that are intersected at the polished surface. Note, however, the complete absence of filamentous morphotypes. The asterisk in (h) indicates the location of Raman spectroscopy analysis (Figure 4). Brt = Barite; CM = carbonaceous matter; Gn = galena; Op = opaline silica (opal-CT); Py = pyrite



of EPS, and relationships with wavy and wrinkly carbonaceous matter layering (Figures 5h, 10a-c and 11). Lastly, whereas metabolisms in deep-marine systems are diverse, and although unambiguous characterizations require genomic and biomarker analyses, it is possible that some of the microbial species observed here are sulfur-metabolizing organisms, which are generally common at sulfidic vents owing to the ubiquitous availability of sulfur compounds (Frank et al., 2013; Jannasch & Mottl, 1985; Jørgensen et al., 1992; Schauer et al., 2011).

### 5.3 | Ambient versus microbial controls on pyrite precipitation and microtextures

The spatial coincidence between microbial features and pyrite raises several questions. Firstly, is this relationship a testimony of causal influence—microbial activity influenced pyrite stability—or solely of ambient parameters promoting their cooccurrence? Specifically, was the precipitation of pyrite actively and/or passively influenced by microbes (?); the former refers to influence by intracellular processes, such as metabolisms, and the latter to controls by organics, such as cellular matter and EPS. Secondly, did microbial activity establish mineral-textural fingerprints that are distinguishable from purely abiotic features?

The pyrite studied here shows strong similarities in terms of micro-mineralogy and microstructure—concentric to laminated corrugated pyrite composed of fibrous nanocrystals aligned normal or in radial orientation (Figures 5e-g and 10a)—compared to previous reports of pyrite formed from deep-marine venting of acidic and Fe- and H<sub>2</sub>S-rich hydrothermal fluids into the water column (e.g. Ikehata et al., 2015; Lehrmann et al., 2015; Xu & Scott, 2005). In such environments of mixing with cold, oxic seawater, the (localized) attainment of (super-) saturation of pyrite in mixed solution is not necessarily controlled by temperature and the availability of reduced Fe and S (H<sub>2</sub>S), but also by pH and redox conditions (and hence sulfur speciation); parameters that generally influence the crystals morphology and aggregation pattern of pyrite (Barrie et al., 2009; Graham & Ohmoto, 1994; Murowchick & Barnes, 1987; Ohfuji & Rickard, 2005; among others). Microbial metabolisms and the properties of organics can further influence redox and pH conditions, the accumulation of metal cations, and hence the stability and textural expression of precipitating iron sulfide (e.g. Duverger et al., 2020; Gorlas et al., 2018; Thiel et al., 2019). However, proximal to the discharge zone of sulfidic black smokers, these biological factors are unlikely to have significance compared to ambient constraints, particularly not the reduced and acidic conditions imparted by hydrothermal fluids, and the steep temperature gradients (undercooling) that can be induced by their mixing with cold and relatively oxygenated seawater. These factors not only influence the precipitation of pyrite (Findlay et al., 2019), but generally promote fibrous crystal growth and a concentric aggregation of crystallites (Gránásy et al., 2005, and references therein). Hence, concerning the pyrite in this study, these

considerations make it likely that ambient conditions (especially temperature) dictated pyrite formation, regardless of the presence of microbes. As such, pyrite precipitation is regarded as an essentially abiogenic process, with overall limited, but not negligible influence of biology on the development of microtextures.

An observation that supports a local influence of biology is the textural heterogeneity of pyrite in the areas of large amounts of carbonaceous matter, that is, particularly where carbonaceous matter is contained as wavy and wrinkly laminae, which occasionally merge into micro-columnar structures (Figures 5h, 7f and 10a-c). This carbonaceous matter layering, which contrasts with the repeating, concentric to corrugated texture of pyrite that is imparted by ambient parameters (Figure 11), resembles wavy and wrinkly biofilm layering, and by extension microbially induced layering in stromatolites formed in sedimentary systems. It is believed that the formation of such biogenic textures is dependent on the interplay of (i) microbial growth dynamics, (ii) rheology of layers of living, dormant, or dead microbial biofilm assemblages (i.e., microorganisms plus EPS, as well as their degraded remains), and (iii) capture and precipitation of minerals (Visscher & Stolz, 2005; Westall et al., 2000). In this study, the hypothesis of biofilm growth influencing the nucleation and aggregation patterns of pyrite is consistent with the close spatial relationships of the wavy to wrinkly carbonaceous pyrite textures to swarms of coccoidal biomorphs plus their carbonaceous matrices, the latter which are reminiscent of connective organic EPS networks (Figures 5h, 7f, 10, 11, and DR3). Therefore, and because comparable textures are entirely absent in other areas, including those that are dominated by filamentous microbes, the wavy to wrinkly laminated carbonaceous pyrite, whose texture differs compared to ordinary pyrite at hydrothermal vents (Figure 11), is consistent with an origin from continuous biofilm growth and a parallel build-up of degrading biomass, although additional contributions from migrated bitumens cannot be entirely ruled out.

### 5.4 | Taphonomy and fossilization of microorganisms

The taphonomy of microorganisms at deep-marine vents, especially preservation by pyritization, is little studied. Notable exceptions are Georgieva et al. (2015) and Georgieva et al. (2018), which report from the pyritized walls of *Alvinella* polychaete tubes the presence of microfossil-bearing, “stromatolite-like” pyrite showing some similarities to the pyrite mineralization observed in this study (compare Figure 5h with Georgieva et al., 2015, their Figure 4b and c). Although these studies do not report evidence for coccoidal microorganisms, they observe filamentous microfossils comparable those in this study, that is, filaments with strikingly similar diameter, shape, and internal microtexture, including segmentation (compare Figures 7a-c and 8a with Georgieva et al., 2015, their Figure 4). Consistent with these accounts, the microfossils studied here appear to be selectively pyritized, that is, as deduced from SEM imagery, the crosswalls/septae, and perhaps

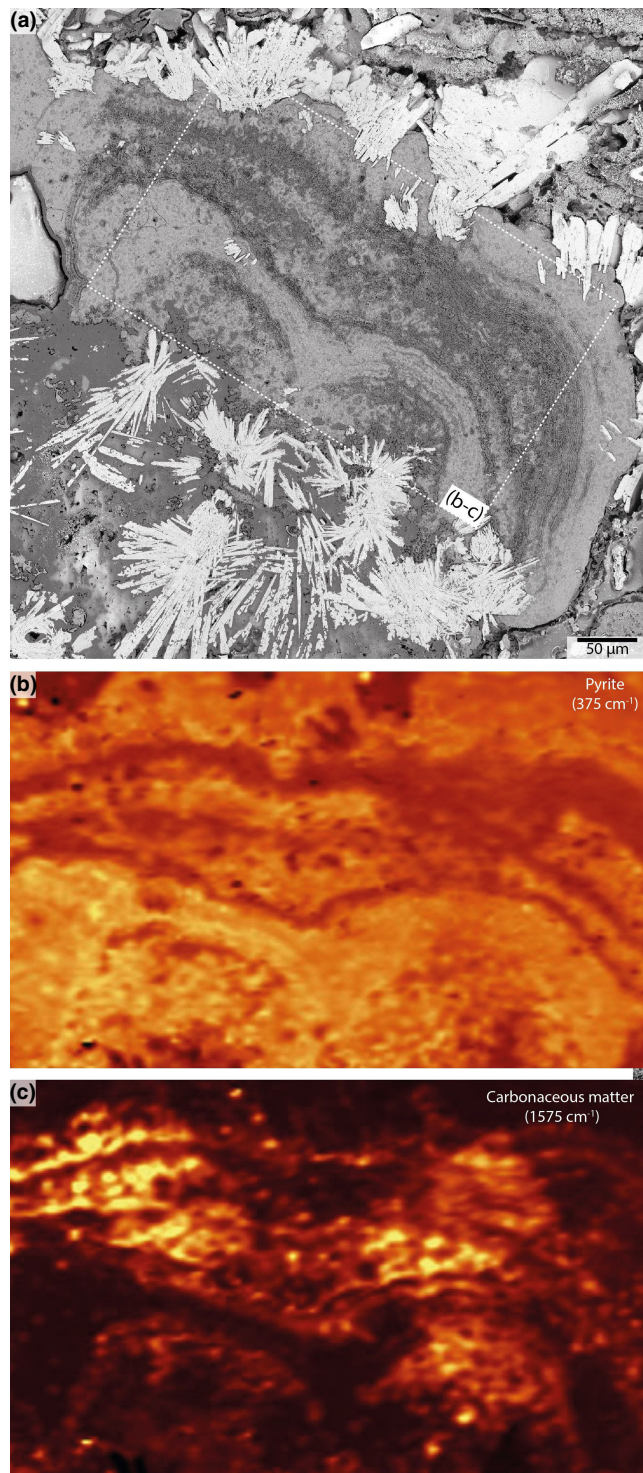


**FIGURE 6** Electron image and Raman spectroscopy maps of colloform pyrite. (a) Backscattered electron (BSE) image of colloform pyrite following nitric acid etching, which exposes opaline silica and carbonaceous matter. Note the irregular to radial aggregates of tabular barite crystals (bright white) below and above the colloform pyrite. (b-c) Raman spectroscopy maps for the  $375\text{ cm}^{-1}$  band of pyrite (b) and  $1575\text{ cm}^{-1}$  band of carbonaceous matter (c); see the Raman spectra of pyrite and carbonaceous matter in Figure 4 for comparison. Note that the map of carbonaceous matter in (c) is found to be free of any interfering signals from epoxy contaminants based on the absence of any (interfering) epoxy signals at  $\sim 820\text{ cm}^{-1}$  and  $1610\text{ cm}^{-1}$  (see the Raman spectrum of epoxy in Figure 4)

microfossil interiors (Figures 8, 9 and Figure S1b). Overall, pyritized filamentous microfossils with silicified interiors are not restricted to hydrothermal systems. One of the earliest accounts comes from the Paleoproterozoic ( $\sim 1.9\text{ Ga}$ ) Gunflint chert, where filaments in what are now strongly silicified sedimentary strata are often preserved as strongly pyritized, tubular sheaths (Wacey et al., 2013). The latter study proposed a multi-stage formation model for such microfossils: (i) perhaps prior to remineralization, a breakdown of the labile cell interiors; (ii) contemporaneous to diagenetic silicification, pyritization of the refractory cell walls and EPS sheaths. The latter is because cellular material possesses abundant anionic carboxyl, hydroxyl, and phosphoryl groups, and thus a high reactivity toward metal cations (Kaplan et al., 1987; Konhauser et al., 1993).

A combination of the above processes, though co-occurring (near-) contemporaneous to microbial growth, can explain the filamentous microfossils studied here, especially their silica in-fills and the pyritization of cellular matter (Figure 8a-b; Fig. S2). However, this model conflicts with the predominately pyritized interiors and the carbonaceous cell walls of the coccoidal microfossils (compare Figure 7a-c with Figure 7d-f). The cause(s) for these differences remain speculative, but in the absence of evidence for the growth and entombment of the filamentous and coccoidal microbes at fundamentally different conditions, an explanation could be that taphonomy was influenced by the microbes themselves. Archaea and bacteria, both which are candidates for the observed microorganisms, show contrasting cell wall compositions: i) those of bacteria contain peptidoglycan (polysaccharide chains linked by peptide bonds); ii) those of archaea are composed of glycoproteins, pure proteins, or pseudopeptidoglycan, which is similar to peptidoglycan but contains different polysaccharide chains (Klingl et al., 2019; Silhavy et al., 2010). Such a difference, and perhaps contrasting metabolisms, would alter the microenvironment surrounding microbes, and thus phase stabilities. Moreover, differences in cell wall composition may influence the binding of metal and non-metal cations (i.e., Fe vs. Si). Understanding such potential dependencies, however, which were explored for the silification (but not pyritization) of archaea and bacteria in Orange et al. (2009) and other studies, will require experiments on microbes for the conditions met at sulfidic hydrothermal vents, that is, immersion in co-saturated iron-sulfide-silica fluids at different increments of temperature and pH.

cell walls and outer sheaths (if preserved and recognizable), are mostly ubiquitously mineralized to pyrite, whereas the interiors are filled by silica.

The studies of Georgieva et al. (2015) and Georgieva et al. (2018) proposed pathways for such styles of microbial entombment, all of which rely on organic matter promoting the conditions necessary for pyrite precipitation, and/or cellular matter templating pyrite aggregation. However, for the microfossils observed in this study, this picture is incomplete without consideration of the silicification of

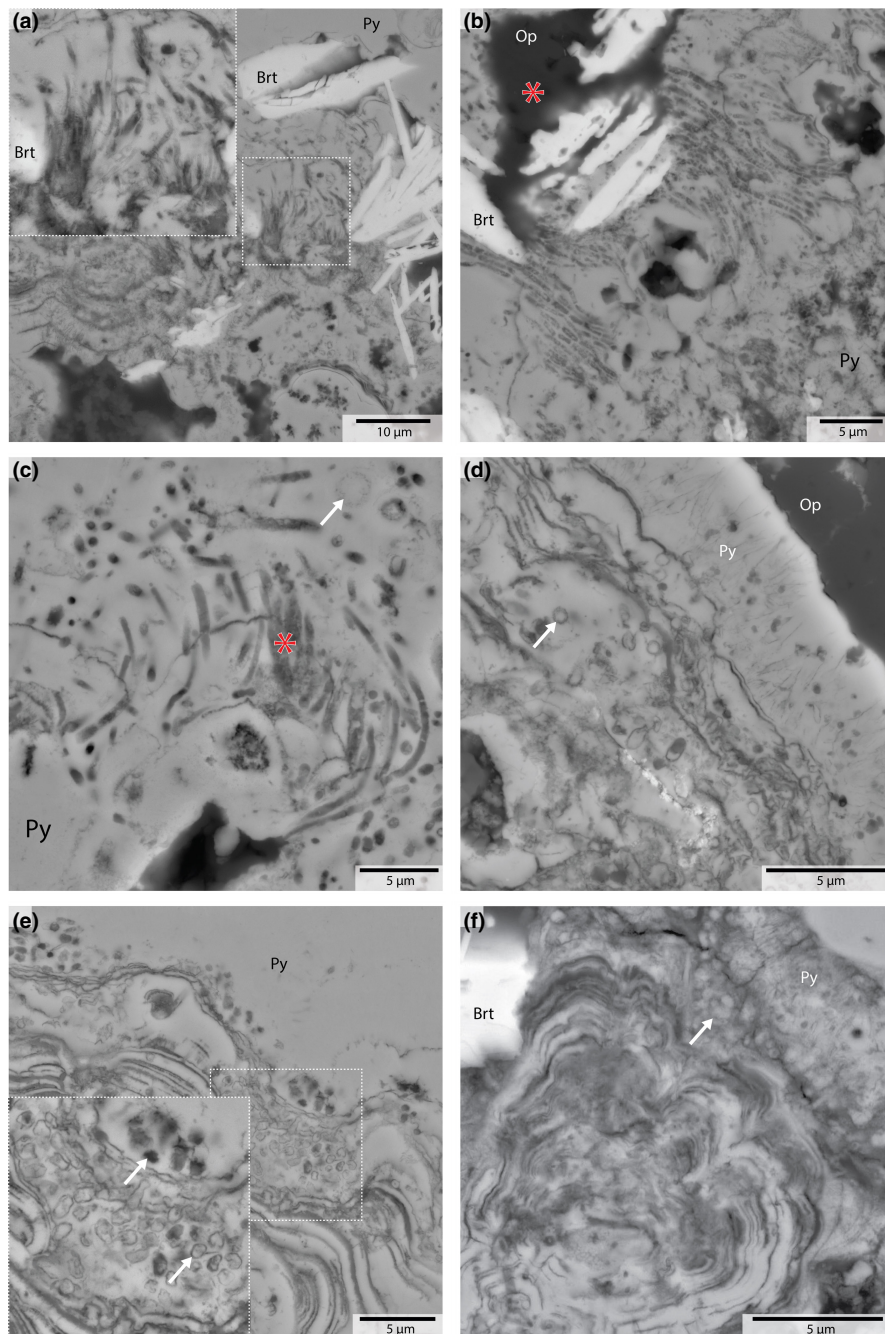


**FIGURE 7** Filamentous and coccoidal morphotypes within colloform and botryoidal pyrite. (a-c) Interlaced or parallel-oriented, filamentous microfossils. The white arrow indicates a putative coccoidal biomorph; compare with (d-f). Loosely to tightly packed swarms of coccoidal biomorphs. The white arrows indicate coccoidal features with or without pyrite-filled interiors. Images (d) and (e) are taken from areas shown in [Figure 5d](#) and [Figure 11](#), respectively. The asterisks in (b) and (c) indicate the location of Raman spectroscopy analysis ([Figure 4a](#)). Brt = Barite; Op = opaline silica (opal-CT); Py = pyrite

Besides these broad constraints on taphonomy, some detailed characteristics of the coccoidal microfossils, especially their pitted appearances ([Figures 8c-d](#) and [10e-f](#)), require further discussion. In the absence of evidence for origins from sample treatment (nitric acid etching) and thermal damage from electron imaging, this pitting may be interpreted in several non-mutually exclusive ways. Firstly, it stems from reproduction, particularly multiple fission. Cell growth and reproduction are usually linked, which could explain the more common perforation of coccoidal microbes above a certain diameter threshold ( $>0.7\text{--}0.8\ \mu\text{m}$ ). However, a shortcoming is that reproduction via multiple fission is perhaps restricted to much larger microorganisms, typically cyanobacteria that are not to be met in deep-marine realms ([Angert, 2005](#)). Secondly, these

microstructures stem from gas vacuoles. However, lipid-lined vesicles of gas, which aid in motility, usually exist in organisms from the water column, especially planktonic cyanobacteria ([Walsby, 1994](#)). Thirdly, they are expelled sulfur vesicles. Previous studies have shown that some archaeal species from deep-sea hydrothermal vents, many which show similar cell volumes and morphological traits compared to the coccoids studied here, may sequester excess sulfur in vesicles ([Gorlas et al., 2015, 2018](#)). Perhaps most likely, however, the pitting may represent indentations from cell membrane dehydration and contraction during fossilization, indentations from precipitating pyrite crystals, or vesicles formed by post-mortem thermal overprint. Indeed, Raman spectroscopy analysis ([Figure 4](#)) indicates that the carbonaceous matter of the

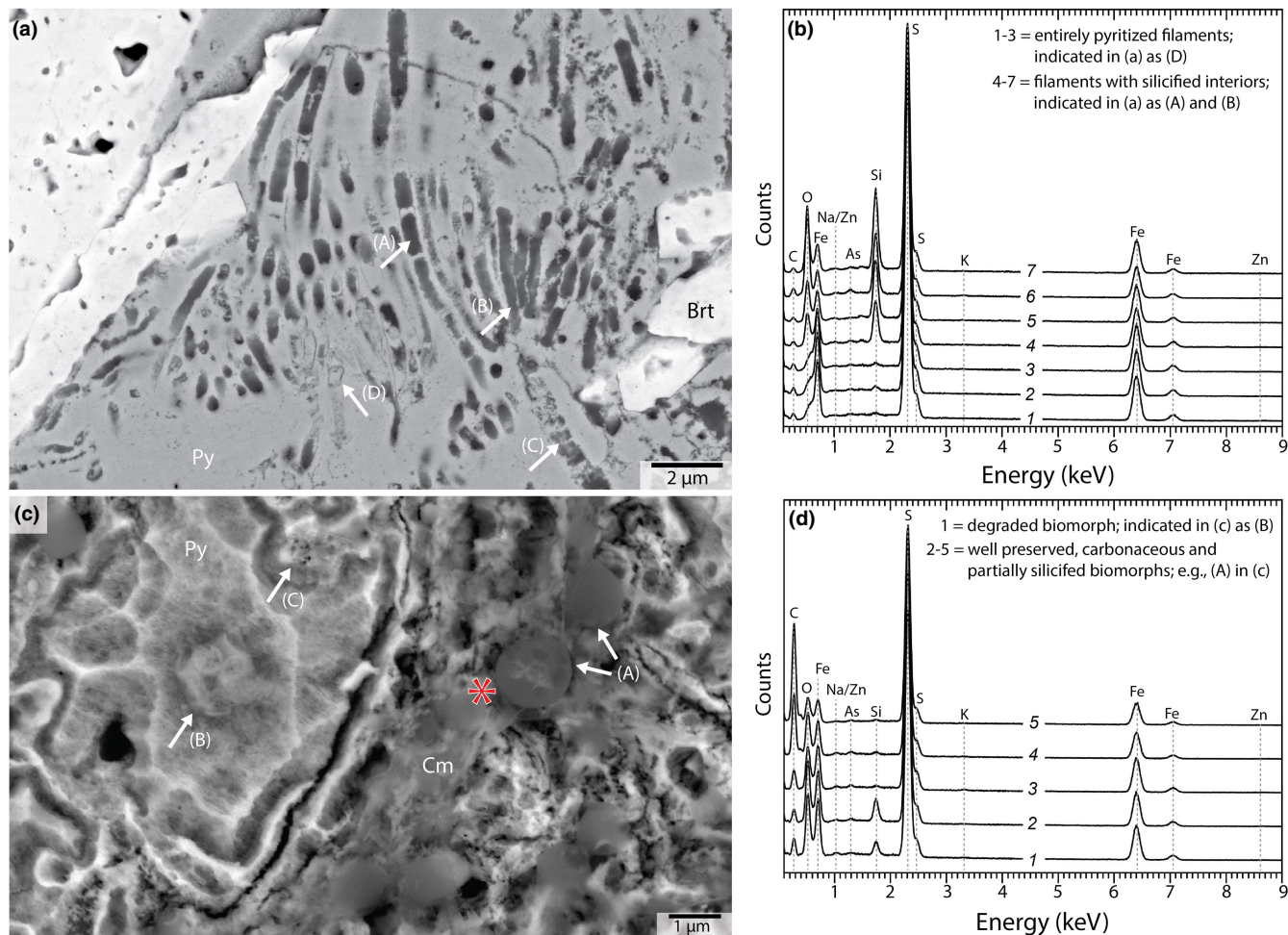


**FIGURE 8** Electron images and elemental analyses (energy dispersive X-ray spectroscopy) of filamentous and coccoidal biomorphs within colloform and botryoidal pyrite. (a) Backscattered electron image of filamentous biomorphs. The arrows indicate various stages and styles of mineralization: (A) Filament with silicified segments and pyritized interstices reminiscent of septae/crosswalls; (B) Filament with silicified interior that shows no segmentation; (C) Segmented filament with a partially pyritized interior. (D) Entirely pyritized filaments. Note for filaments (A) and (C) the subtle difference in segmentation, that is, the latter is a rare example that potentially shows relatively narrower spaced segmentation. It is unclear whether this disparity relates to original differences among the filaments, or to contrasting crystallization patterns of pyrite in the interiors. (b) Elemental analysis of the filamentous biomorphs shown in (a). See for comparison the EDS elemental distribution maps in Fig. S2. (c) Image of well-preserved coccoidal biomorphs in pyrite. The white arrows indicate different stages of coccoidal biomorph degradation and remineralization: (A) well-preserved biomorph with pitting; (B) strongly degraded biomorph with pitting; (C) vanished biomorph, denoted by a core of rounded pyrite and a corrosion halo from acid etching. Elemental distribution maps of the imaged area are shown in Fig. S3. (d) Elemental analysis of some of the coccoidal features shown in (c). The asterisk in (c) indicates the location of Raman spectroscopy analysis (Figure 4). Brt = barite; CM = carbonaceous matter; Py = pyrite

microfossils experienced mild heating, which may have led to the formation and trapping of vesicles.

## 5.5 | Implications for micropaleontology and detecting traces of ancient life

This study expands the understanding of microbial preservation in hydrothermal settings, in particular the structure-preserving precipitation of pyrite and silica, both at the scales of individual microorganisms and putative biofilm assemblages (Figure 11). The only unambiguous account of similar mineralization from comparable

environments in the ancient rock record are those reported in Georgieva et al. (2018) from 440 Ma hydrothermal sulfide deposits. The in part exquisite preservation of microfossils in this example relates to limited hydrothermal and metamorphic overprinting after initial formation. By comparison, preservation in more strongly altered materials is presumably scale dependent. Micron-scale microfossils are perhaps most prone to destruction (e.g., via recrystallization), whereas whole biofilm assemblages, irrespective of whether they occur at the scale of tens of microns or millimeters and centimeters, have a better textural preservation potential despite being equally susceptible to mineralogical and chemical alteration as well as loss of organic content. As degradations advance, a key to the identification

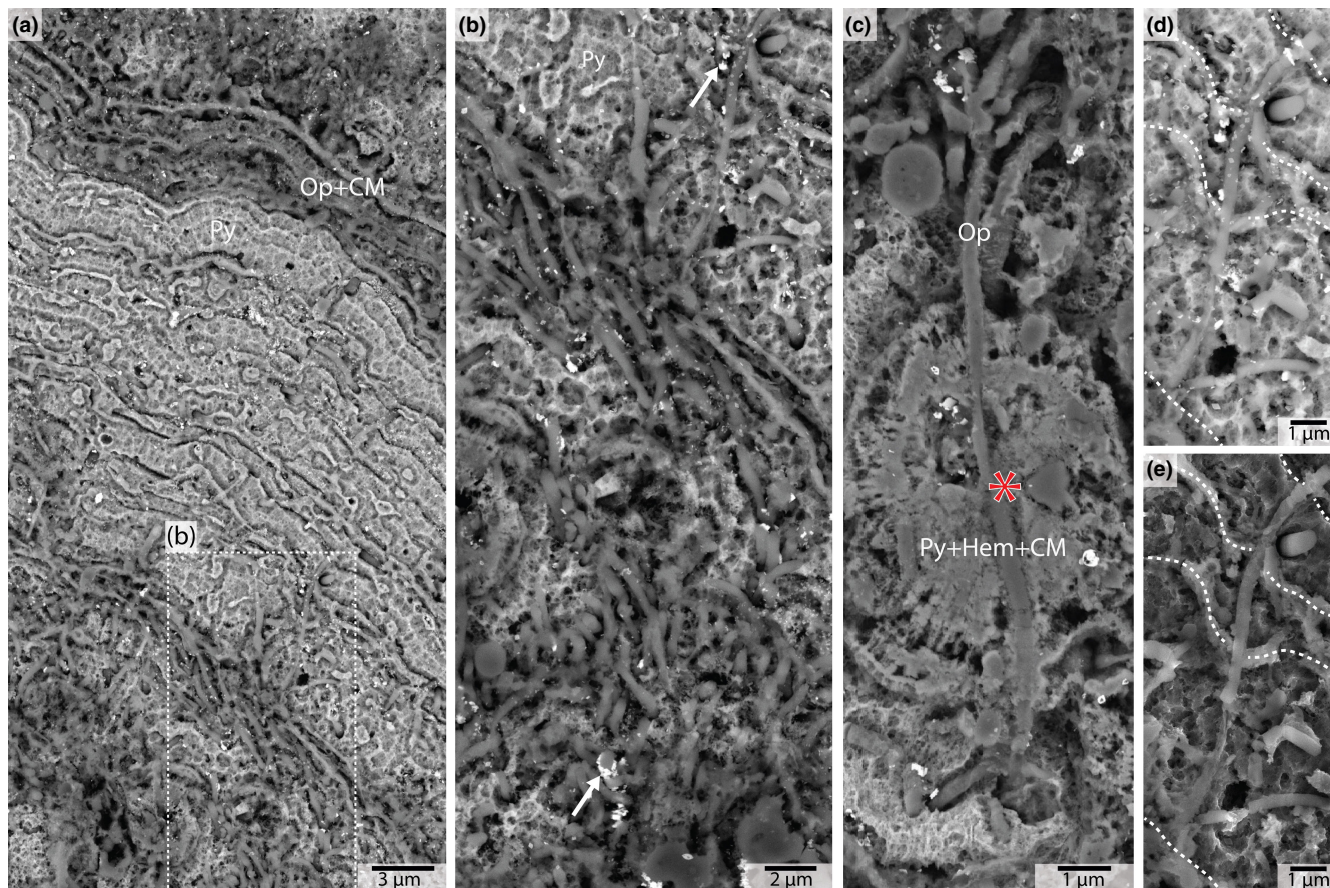


**FIGURE 9** Filamentous biomorphs following nitric acid etching of the pyrite host. All images [a-d = backscattered electron (BSE); (e) = secondary electron (SE)] are taken from the colloform pyrite in Figure 6. Note in (a) the corrugated fine-scale lamination of the colloform pyrite. Image (b) shows an area of partially interlaced, strongly silicified filaments, each which are  $<1\ \mu\text{m}$  in diameter. The white arrows indicate  $\text{Pb} \pm \text{As}$ -rich mineral grains (determined in EDS analysis; not shown here). Image (c) shows a filament following nitric acid etching represented by its corrosion-resistant, silicified interior that transects a radial-fibrous, circular aggregate. Raman spectroscopy analysis indicates that the dull material associated with the latter is hematized. Images (d) and (e) show a filament that transects pyrite layering (white dashed lines). The asterisk in (c) indicates the locations of Raman spectroscopy analysis (Figure 4). CM = carbonaceous matter; Hem = hematite; Op = opaline silica; Py = pyrite

of fossil biofilm microtextures may be to contrast them with cogenetic, truly abiotic rock and mineral fabrics in the immediate surroundings (see discussion above and Figure 11), as is also routinely carried out at a larger scale for fossil microbial mats in ancient sedimentary rocks, especially Archean and Proterozoic stromatolites (e.g., Van Kranendonk et al., 2019).

Hence, we advocate that low-temperature sulfide mineralization of hydrothermal settings, particularly colloform and botryoidal pyrite, requires characterization above routine approaches. For example, several studies on mineralization that are potentially similar to those studied here have lacked microtextural and micro-mineralogical characterization, as well as Raman spectroscopy analysis for carbonaceous matter at sufficiently small scale; see, for example, Rasmussen (2000, their Figure 2) and Present et al. (2017, their Figure 8). The importance of such detailed analyses was recently demonstrated for the pyritized stromatolites from the 3.48 Ga Dresser Formation. Microtextural analysis, together with mineralogical and chemical characterizations down to the nanoscale, provided insights into the putative interplay between microbes and

(near-) syndepositional hydrothermalism/pyrite precipitation, and how the latter influenced the preservation of microtextures and carbonaceous remains that are interpreted as biogenic (Baumgartner, Caruso, et al., 2020; Baumgartner, Van Kranendonk, et al., 2020; Baumgartner et al., 2019). Besides this, additional work remains to be conducted on pyritized biofilm and microbial mat features in hydrothermally influenced deposits from a variety of settings (e.g., shallow marine vs. deep-marine; Si-rich vs. Si-poor vent fluids) to further understand differences in biofilm preservation and microfossil taphonomy (e.g., casting vs. replacement; carbonization vs. silification and pyritization) relative to environment-specific variables, such as temperature and fluid chemistry, including pH and redox conditions.

## 6 | CONCLUDING REMARKS

This study describes microstructures in a recent sulfidic deep-sea hydrothermal vent (black smoker) that are interpreted as fossilizations

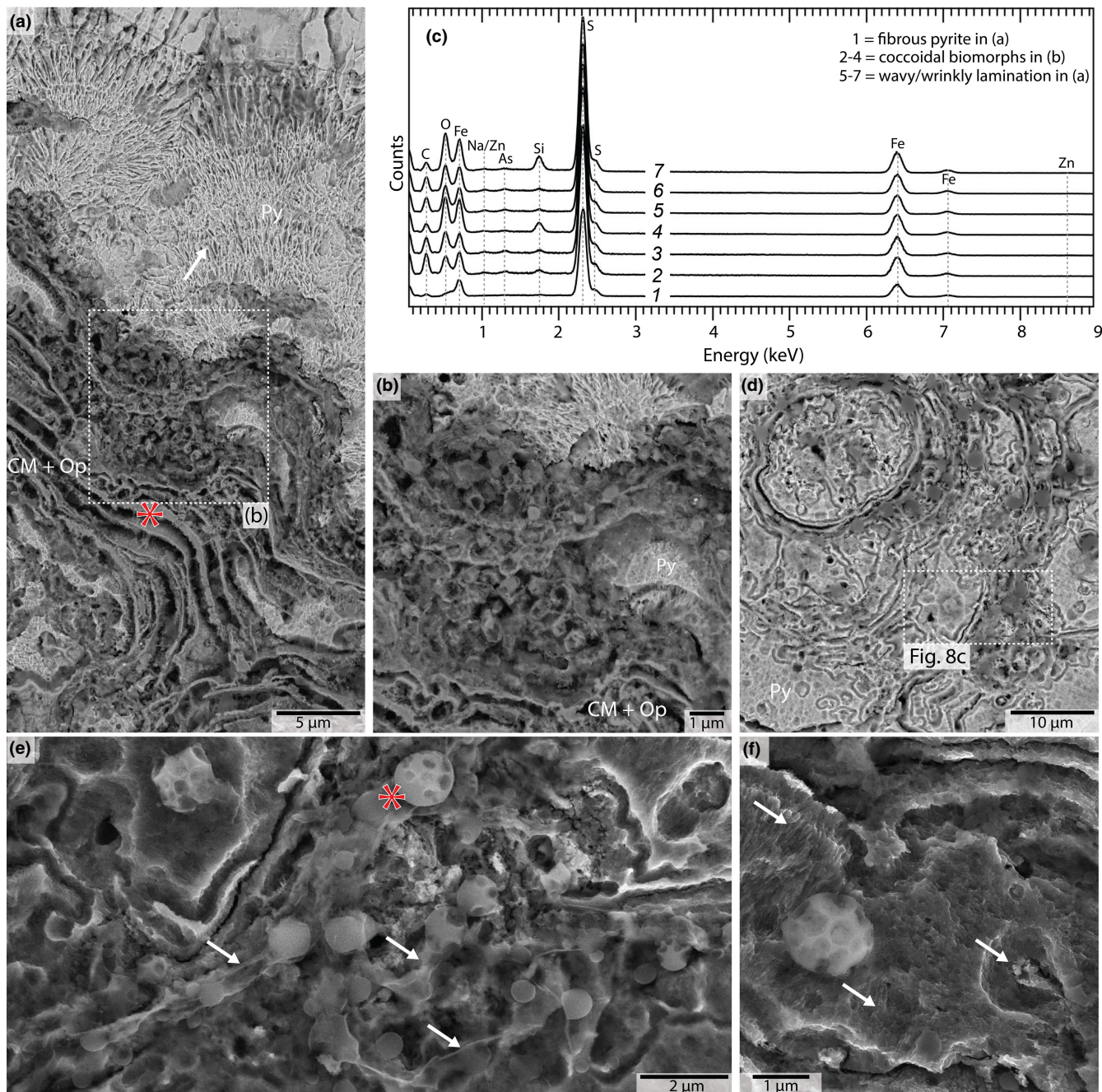


**FIGURE 10** Coccolidal biomorphs following nitric acid etching of the pyrite host. (a–b) Swarms of well to poorly preserved coccolidal forms associated with wavy and wrinkly laminae of carbonaceous matter plus opaline silica. Note in (a) the absence of discernible biomorphs in the lower, smoother carbonaceous matter laminae, which perhaps relates to consecutive growth, lamina by lamina, accompanied by accumulation of biomass as well as compaction and degradation of biomorphs. See for (a) and (b) the same area prior to nitric acid etching in [Figures 7e](#) and [11](#). White arrow in (a) indicates the radial-fibrous texture of pyrite. (c) Elemental analysis of pyrite and carbonaceous features in (a) and (b). (d–f) Electron images [(d) = BSE image; (e–f) = SE images] of well-preserved coccolidal forms. Note in (e) and (f) the distinctive pitting, which is mostly restricted to entities with >0.8–1.0 μm diameter. The image (e), which was acquired on assemblages of coccolidal biomorphs in (d), shows smooth or ropey carbonaceous matter sheaths (white arrows) that may represent fossil EPS. The left arrow in (f) indicates the fibrous habit of pyrite. The right arrows indicate molds that likely relate to vanished coccolidal biomorphs. Elemental distribution maps of the area in (e) are shown in [Fig. S3](#). They further outline the distributions of coccolidal biomorphs and associated carbonaceous matter sheaths. CM = carbonaceous matter; Op = opaline silica; Py = pyrite

of thermophilic microorganisms. The lessons learned about habitability and taphonomy, as well as the interplay between microbial activity and mineral precipitation, have implications for deciphering

the interplay of biological and geological processes in hydrothermally influenced environments preserved in the ancient rock record. The sphalerite-dominated mineralogy of the examined chimney

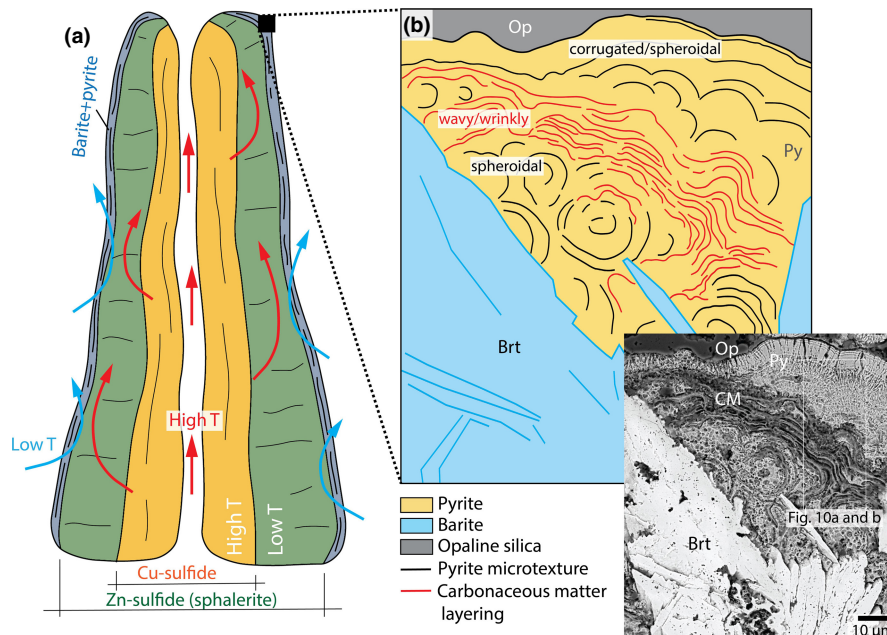


**FIGURE 11** Relationships between fluid evolution, mineral precipitation, and microbial activity in a deep-marine sulfidic chimney. (a) Simplified illustration of the variation of sulfide mineralogy across a sulfide chimney from the Roman Ruins black smokers (not drawn to scale). Compared to the inner, high-temperature zones dominated by Cu-sulfide and then Zn-sulfide (sphalerite), microbial activity is restricted to outer zones, where vigorous mixing between fluids—that is, between hot, reduced, and sulfidic hydrothermal fluids (red arrows) and cold, oxic seawater (blue arrows)—mediates barite-pyrite precipitation at life-sustaining conditions ( $<120^{\circ}\text{C}$ ). (b) Snapshot of the relationship between barite-pyrite precipitates and putative biofilm features. Note the coherent laminae of carbonaceous matter plus opaline silica, which, compared to the concentric and corrugated textures of the surrounding pyrite, show a distinct, wavy to wrinkly micromorphology. This, and the presence of intimately associated coccoidal forms (see the high-resolution images in [Figure 10a-c](#)), provides evidence that this distinctive carbonaceous matter-rich layering represents a microbially induced feature. Brt = barite; CM = carbonaceous matter; Op = opaline silica; Py = pyrite

material is consistent with sulfide precipitation at temperatures prohibiting life ( $>120^{\circ}\text{C}$ ). However, permineralized (pyritized and silicified) remains of what we interpret as filamentous and coccoidal microbes occur within the outer zones of barite plus carbonaceous matter-rich colloform pyrite, an association indicative for microbial activity coeval to the mixing between hot hydrothermal fluids and cold seawater.

Further to previous studies, we show that a rapid precipitation of pyrite and silica in such environments is a suitable process for microbial preservation, with subtle but significant taphonomic differences between the observed microfossil types: (i) for coccoidal microbes, a variable silicification and pyritization of the interiors, and a generally better preservation of the cell walls; (ii) for filamentous microbes, mostly a strong pyritization of the cell walls, but a silicification (and much lesser pyritization) of the interiors. Besides microenvironmental controls, potential factors contributing to such differences may be contrasting metabolisms and contrasting cell chemistries, such as compositionally different cell walls of bacteria and archaea, and thus deviating reactivities toward metal and non-metal cations, that is, Fe versus Si, implicated in pyritization and silicification, respectively.

A notable observation is that the examined vent microbiota, some which may represent biofilm-forming microorganisms, could have contributed to the formation of carbonaceous microtextures

typical for biological mediation, that is, other than the repeating textures of finely laminated colloform and botryoidal pyrite, more heterogeneous, wavy, and wrinkly features, and locally also micro-columnar growth forms. Hence, our work supports the hypothesis that microtextures of pyritized microbiota from hydrothermal realms can have a similar significance as those from purely sedimentary environments. Exploring this possibility further will require a rigorous (re-) examination of microbial (-like) sulfide mineralization of comparable, though not necessarily identical hydrothermal provenance (e.g., deep vs. shallow marine).

#### ACKNOWLEDGMENTS

The authors acknowledge the facilities and the scientific and technical assistance of the Australian Microscopy & Microanalysis Research Facility at Centre for Microscopy, Characterization and Analysis (UWA). Julien Bourdet (CSIRO Energy) is acknowledged for access to the Raman spectroscopy laboratory and his help with data acquisition. Kevin Lepot and Kurt Konhauser are acknowledged for editorial handling, and three anonymous reviewers are thanked for providing constructive comments.

#### DATA AVAILABILITY STATEMENT

The data that support the findings of this study are available from the corresponding author upon reasonable request.

## REFERENCES

- Al-Hanbali, H., Sowerby, S. J., & Holm, N. G. (2001). Biogenicity of silicified microbes from a hydrothermal system: relevance to the search for evidence of life on earth and other planets. *Earth and Planetary Science Letters*, 191, 213–218. [https://doi.org/10.1016/S0012-821X\(01\)00421-6](https://doi.org/10.1016/S0012-821X(01)00421-6)
- Angert, E. R. (2005). Alternatives to binary fission in bacteria. *Nature Reviews Microbiology*, 3, 214–224.
- Barrie, C. D., Boyce, A. J., Boyle, A. P., Williams, P. J., Blake, K., Ogawara, T., Akai, J., & Prior, D. J. (2009). Growth controls in colloform pyrite. *American Mineralogist*, 94, 415–429. <https://doi.org/10.2138/am.2009.3053>
- Baumgartner, R. J., Caruso, S., Fiorentini, M. L., Van Kranendonk, M. J., Martin, L., Jeon, H., Pages, A., & Wacey, D. (2020). Sulfidization of 3.48 billion-year-old stromatolites of the Dresser Formation, Pilbara Craton: Constraints from in-situ sulfur isotope analysis of pyrite. *Chemical Geology*, 537, 119488.
- Baumgartner, R. J., Van Kranendonk, M. J., Fiorentini, M. L., Pages, A., Wacey, D., Kong, C., Saunders, M., & Ryan, C. (2020). Formation of micro-spherulitic barite in association with organic matter within sulfidized stromatolites of the 3.48 billion-year-old Dresser Formation, Pilbara Craton. *Geobiology*, 18, 415–425. <https://doi.org/10.1111/gbi.12392>
- Baumgartner, R. J., Van Kranendonk, M. J., Wacey, D., Fiorentini, M. L., Saunders, M., Caruso, S., Pages, A., Homann, M., & Guagliardo, P. (2019). Nano-porous pyrite and organic matter in 3.5-billion-year-old stromatolites record primordial life. *Geology*, 47, 1039–1043. <https://doi.org/10.1130/G46365.1>
- Binns, R. A. (2014). Bikpela: a large siliceous chimney from the PACMANUS hydrothermal field, Manus basin, Papua New Guinea. *Economic Geology*, 109, 2243–2259. <https://doi.org/10.2113/econgeo.109.8.2243>
- Binns, R. A., McConachy, T. F., Parr, J. M., & Yeats, C. J. (2002). *The PACMANUS Memoir (P2+)*. CSIRO Exploration and Mining Report 1032C.
- Bower, D. M., Hummer, D. R., & Steele, A. (2017). An experimental look at the taphonomy of cyanobacterial mats in siliclastic sediments. *Palaeos*, 32, 725–738. <https://doi.org/10.2110/palo.2017.016>
- Briggs, D. E. G., Bottrell, S. H., & Raiswell, R. (1991). Pyritization of soft-bodied fossils: Beecher's Trilobite Bed, Upper Ordovician, New York State. *Geology*, 19, 1221–1224. [https://doi.org/10.1130/0091-7613\(1991\)019<1221:POSBFB>2.3.CO;2](https://doi.org/10.1130/0091-7613(1991)019<1221:POSBFB>2.3.CO;2)
- Cosmidis, J., Benzerara, K., Menguy, N., & Arning, E. (2013). Microscopy evidence of bacterial microfossils in phosphorite crusts of the Peruvian shelf: Implications for phosphogenesis mechanisms. *Chemical Geology*, 359, 10–22. <https://doi.org/10.1016/j.chemgeo.2013.09.009>
- Curtis, N. J., Gascooke, J. R., Johnston, M. R., & Pring, A. (2019). A review of the classification of opal with reference to recent new localities. *Minerals*, 9, 299. <https://doi.org/10.3390/min9050299>
- Duveger, A., Berg, J. S., Busigny, V., Guyot, F., Bernard, S., & Miot, J. (2020). Mechanisms of pyrite formation promoted by sulfate-reducing bacteria in pure culture. *Frontiers in Earth Science*, 8, 457.
- Findlay, A. J., Estes, E. R., Gartman, A., Yucel, M., Kamyshny, J. R., & Luther, G. W. III. (2019). Iron and sulfide nanoparticle formation and transport in nascent hydrothermal vent plumes. *Nature Communications*, 10, 1597.
- Frank, K. L., Rogers, D. R., Olins, H. C., Vidoudez, C., & Girguis, P. R. (2013). Characterizing the distribution and rates of microbial sulfate reduction at Middle Valley hydrothermal vents. *The ISME Journal*, 7, 1391–1401. <https://doi.org/10.1038/ismej.2013.17>
- Georgieva, M. N., Little, C. T. S., Bailey, R. J., Ball, A. D., & Glover, A. G. (2018). Microbial-tubeworm associations in a 440 million year old hydrothermal vent community. *Proceedings Royal Society B Biological Science*, 285, 20182004. <https://doi.org/10.1098/rspb.2018.2004>
- Georgieva, M. N., Little, C. T. S., Ball, A. D., & Glover, A. G. (2015). Mineralization of Alvinella polychaete tubes at hydrothermal vents. *Geobiology*, 13, 152–169.
- Gorlas, A., Jacquemot, P., Guigner, J. M., Gill, S., Forterre, P., & Guyot, F. (2018). Greigite nanocrystals produced by hyperthermophilic archaea of Thermococcales order. *PLoS One*, 13, 8. <https://doi.org/10.1371/journal.pone.0201549>
- Gorlas, A., Marguet, E., Gill, S., Geslin, C., Guigner, J.-M., Guyot, F., & Forterre, P. (2015). Sulfur vesicles from Thermococcales: A possible role in sulfur detoxifying mechanisms. *Biochimie*, 118, 356–364. <https://doi.org/10.1016/j.biochi.2015.07.026>
- Graham, U.M., & Ohmoto, H. (1994). Experimental study of formation mechanisms of hydrothermal pyrite. *Geochimica Et Cosmochimica Acta*, 58, 2187–2202. [https://doi.org/10.1016/0016-7037\(94\)90004-3](https://doi.org/10.1016/0016-7037(94)90004-3)
- Gránásky, L., Pusztai, T., Tegze, G., Warren, J. A., & Douglas, J. F. (2005). Growth of Spherulites. *Physical Review E*, 72, 011605.
- Griffith, E. M., & Paytan, A. (2012). Barite in the ocean - occurrence, geochemistry and paleoceanic applications. *Sedimentology*, 59, 1817–1835.
- Henry, D. G., Jarvis, I., Gillmore, G., & Stephenson, M. (2019). Raman spectroscopy as a tool to determine the thermal maturity of organic matter: Application to sedimentary, metamorphic and structural geology. *Earth-Science Reviews*, 198, 102936. <https://doi.org/10.1016/j.earscirev.2019.102936>
- Hu, S. Y., Barnes, S. J., Glenn, A. M., Pagès, A., Parr, J. M., MacRae, C., & Binns, R. (2019). Growth history of spherulite in a modern seafloor hydrothermal chimney revealed by electron backscattered diffraction. *Economic Geology*, 114, 165–176. <https://doi.org/10.5382/econgeo.2019.4626>
- Huber, J. A., Mark Welch, D. B., Morrison, H. G., Huse, S. M., Neal, P. R., Butterfield, D. A., & Sogin, M. L. (2007). Microbial population structures in the deep marine biosphere. *Science*, 318, 97–100. <https://doi.org/10.1126/science.1146689>
- Ikehata, K., Suzuki, R., Shimada, K., Ishibashi, J., & Urabe, T. (2015). Mineralogical and geochemical characteristics of hydrothermal minerals collected from hydrothermal vent fields in the Southern Mariana spreading center. In J. Ishibashi, K. Okino, & M. Sunamura (Eds.), *Subseafloor Biosphere Linked to Hydrothermal Systems*. Springer.
- Jamieson, J. W., Hannington, M. D., Tivey, M. K., Hansteen, T., Williamson, N. B., Stewart, M., Fietzke, J., Butterfield, D., Frische, M., Allen, L., Cousens, B., & Langer, J. (2016). Precipitation and growth of barite within hydrothermal vent deposits from Endeavour Segment, Juan de Fuca Ridge. *Geochimica Et Cosmochimica Acta*, 173, 65–85.
- Jannasch, H. W., & Mottl, M. J. (1985). Geomicrobiology of deep-sea hydrothermal vents. *Science*, 29, 717–725. <https://doi.org/10.1126/science.229.4715.717>
- Javaux, E. J., & Lepot, K. (2018). The Paleoproterozoic fossil record: Implications for the evolution of the biosphere during Earth's middle-age. *Earth-Science Reviews*, 176, 68–86. <https://doi.org/10.1016/j.earscirev.2017.10.001>
- Jones, B., & Renaut, R. W. (2003). Hot spring and geyser sinters: the integrated product of precipitation, replacement, and deposition. *Canadian Journal of Earth Sciences*, 40, 1549–1569. <https://doi.org/10.1139/e03-078>
- Jørgensen, B. B., Isaksen, M. F., & Jannasch, H. W. (1992). Bacterial sulfate reduction above 100 °C in Deep-Sea Hydrothermal Vent Sediments. *Science*, 258, 1756–1757. <https://doi.org/10.1126/science.258.5089.1756>
- Kaplan, D., Christiaan, D., & Arad, S. (1987). Chelating properties of extracellular polysaccharide from *Chlorella* spp. *Applied and Environmental Microbiology*, 53, 2953–2956.
- Kashefi, K., & Lovley, D. R. (2003). Extending the upper temperature limit for life. *Science*, 301, 934–937. <https://doi.org/10.1126/science.1086823>

- Kimura, H., Asada, R., Masta, A., & Naganuma, T. (2003). Distribution of microorganisms in the subsurface of the Manus Basin hydrothermal vent field in Papua New Guinea. *Applied and Environmental Microbiology*, 69, 644–648. <https://doi.org/10.1128/AEM.69.1.644-648.2003>
- Klingl, A., Pickl, C., & Flechsler, J. (2019). Archaeal cell walls. *Subcellular Biochemistry*, 92, 471–493.
- Konhauser, K. O., Fyfe, W. S., Ferris, F. G., & Beveridge, T. J. (1993). Metal sorption and mineral precipitation by bacteria in two Amazonian river systems: Rio Solimoes and Rio Negro, Brazil. *Geology*, 21, 1103–1106.
- Konhauser, K., Jones, B., Phoenix, V., Ferris, F. G., & Renaut, R. (2005). The microbial role in hot spring silicification. *AMBIO: A Journal of the Human Environment*, 33, 552–558. <https://doi.org/10.1579/0044-7447-33.8.552>
- Le Bris, N., Anderson, L., Chever, F., & Gaill, F. (2008). Sulfide diffusion and chemoautotrophy requirements in an extremophilic worm tube. In L. P. Mertens (Ed.), *Biological oceanography research trends*. Nova Science Publishers.
- Lehrmann, B., Stobbs, I. J., Lutsy, P. A. J., & Murton, B. J. (2015). Insights into extinct seafloor massive sulfide mounds at the TAG, Mid-Atlantic Ridge. *Minerals*, 8, 302. <https://doi.org/10.3390/min8070302>
- Lepot, K. (2020). Signatures of early microbial life from the Archean (4 to 2.5 Ga) eon. *Earth Science Reviews*, 209, 103286.
- Li, J., & Kusky, T. (2001). World's largest known Precambrian fossil black smoker chimneys and associated microbial vent communities, North China: Implications for early life. *Gondwana Research*, 12, 84–100. <https://doi.org/10.1016/j.gr.2006.10.024>
- Little, C. T. S., Cann, J. R., Herrington, R. J., & Morisseau, M. (1999). Late Cretaceous hydrothermal vent communities from the Troodos ophiolite, Cyprus. *Geology*, 27, 1027–1030. [https://doi.org/10.1130/0091-7613\(1999\)027<1027:LCHVCF>2.3.CO;2](https://doi.org/10.1130/0091-7613(1999)027<1027:LCHVCF>2.3.CO;2)
- Luef, B., Frischkorn, K. R., Wrighton, K. C., Holman, H. Y. N., Birarda, G., Thomas, B. C., Singh, A., Williams, K. H., Siegerist, C. E., Tringe, S. G., Downing, K. H., Comolli, L. R., & Banfield, J. F. (2015). Diverse uncultivated ultra-small bacterial cells in groundwater. *Nature Communications*, 6, 6372. <https://doi.org/10.1038/ncomms7372>
- Lutz, R. A., & Kennish, M. J. (1993). Ecology of deep-sea hydrothermal vent communities: A review. *Reviews of Geophysics*, 31, 211–242. <https://doi.org/10.1029/93RG01280>
- Marshall, C. P., Dufresne, W. J. B., & Rufledt, C. J. (2020). Polarized Raman spectra of hematite and assignment of external modes. *Journal of Raman Spectroscopy*, 51, 1522–1529. <https://doi.org/10.1002/jrs.5824>
- Martin, W., Baross, J., Kelley, D. S., & Russell, M. (2008). Hydrothermal vents and the origin of life. *Nature Reviews Microbiology*, 6, 805–814. <https://doi.org/10.1038/nrmicro1991>
- Martinez, F., & Taylor, B. (1996). Backarc spreading, rifting, and microplate rotation, between transform faults in the Manus Basin. *Marine Geophysical Research*, 18, 203–224. <https://doi.org/10.1007/BF00286078>
- McCollom, T. M., & Shock, E. L. (1997). Geochemical constraints on chemolithoautotrophic metabolism by microorganisms in seafloor hydrothermal systems. *Geochimica Et Cosmochimica Acta*, 61, 4375–4391. [https://doi.org/10.1016/S0016-7037\(97\)00241-X](https://doi.org/10.1016/S0016-7037(97)00241-X)
- Meier, D. V., Pjevac, P., Bach, W., Markert, S., Schweder, T., Jamieson, J., Petersen, S., Amann, R., & Meyerdierks, A. (2019). Microbial metal-sulfide oxidation in inactive hydrothermal vent chimneys suggested by metagenomic and metaproteomic analyses. *Environmental Microbiology*, 21, 682–701. <https://doi.org/10.1111/1462-2920.14514>
- Merino, N., Aronson, H. S., Bojanova, D. P., Feyhl-Buska, J., Wong, M. L., Zhang, S., & Giovannelli, D. (2019). Living at the extremes: Extremophiles and the limits of life in a planetary context. *Frontiers in Microbiology*, 10, 780. <https://doi.org/10.3389/fmicb.2019.00780>
- Mullineaux, L. S., Metaxas, A., Beaulieu, S. E., Bright, M., Gollner, S., Grupe, B. M., Herrera, S., Kellner, J. B., Levin, L. A., Mitarai, S., Neubert, M. G., Thurnherr, A. M., Tunnicliffe, V., Watanabe, H. K., & Won, Y. I. (2018). Exploring the ecology of deep-sea hydrothermal vents in a metacommunity framework. *Frontiers in Marine Science*, 5, 1–27. <https://doi.org/10.3389/fmars.2018.00049>
- Murowchick, J., & Barnes, H. L. (1987). Effects of temperature and supersaturation on pyrite morphology. *American Mineralogist*, 72, 1233–1242.
- Nakagawa, S., & Takai, K. (2008). Deep-sea vent chemoautotrophs: diversity, biochemistry and ecological significance. *FEMS Microbiology Ecology*, 65, 1–14. <https://doi.org/10.1111/j.1574-6941.2008.00502.x>
- Nakagawa, S., Takai, K., Inagaki, F., Chiba, H., Ishibashi, J., Kataoka, S., Hirayama, S., Nunoura, T., Hirokoshi, K., & Sako, Y. (2005). Variability in microbial community and venting chemistry in a sediment-hosted backarc hydrothermal system: Impacts of sub-seafloor phase-separation. *FEMS Microbial Ecology*, 54, 141–155. <https://doi.org/10.1016/j.femsec.2005.03.007>
- Nercessian, O., Bienvenu, N., Moreira, D., Prieur, D., & Jeanthon, C. (2005). Diversity of functional genes of methanogens, methanotrophs and sulfate reducers in deep-sea hydrothermal environments. *Environmental Microbiology*, 7, 118–132. <https://doi.org/10.1111/j.1462-2920.2004.00672.x>
- Nims, C., Lafond, J., Alleon, J., Templeton, A. S., & Cosmidis, J. (2021). Organic biomorphs may be better preserved than microorganisms in early Earth sediments. *Geology*, 49, 629–634. <https://doi.org/10.1130/G48152.1>
- Ohfuji, H., & Rickard, D. (2005). Experimental syntheses of framboids - a review. *Earth Science Reviews*, 71, 147–170. <https://doi.org/10.1016/j.earscirev.2005.02.001>
- Orange, F., Westall, F., Disnar, J. R., Prieur, D., Bienvenu, N., Le Romancer, M., & Défarge, C. (2009). Experimental silicification of the extremophilic Archaea *Pyrococcus abyssi* and *Methanocaldococcus jannaschii*: applications in the search for evidence of life in early Earth and extraterrestrial rocks. *Geobiology*, 7, 403–418.
- Park, C. B., & Clark, D. S. (2002). Rupture of the cell envelope by decompression of the deep-sea methanogen *Methanococcus jannaschii*. *Applied Environmental Microbiology*, 68, 1458–1463.
- Paterson, D. J., De Jonge, M. D., Howard, D. L., Lewis, W., McKinlay, J., Starritt, A., Kusel, M., Ryan, C. G., Kirkham, R., Moorhead, G., & Siddons, D. P. (2011). The X-ray fluorescence microscopy beamline at the Australian synchrotron. *AIP Conference Proceedings*, 1365, 219–222.
- Present, T. M., Bergmann, K. D., Myers, C., Slotznick, S. P., Creveling, J. R., Zieg, J., Fischer, W. W., Knoll, A. H., & Grotzinger, J. P. (2017). Pyrite-walled tube structures in a Mesoproterozoic sediment-hosted metal sulfide deposit. *GSA Bulletin*, 130, 598–616. <https://doi.org/10.1130/B31504.1>
- Rasmussen, B. (2000). Filamentous microfossils in a 3,235-million-year-old volcanogenic massive sulphide deposit. *Nature*, 405, 676–679. <https://doi.org/10.1038/35015063>
- Reeves, E. P., Seewald, J. S., Saccocia, P., Bach, W., Craddock, P. R., Shanks, W. C., Sylva, S. P., Walsh, E., Pichler, T., & Rosner, M. (2011). Geochemistry of hydrothermal fluids from the PACMANUS, Northeast Pual and Vienna Woods hydrothermal fields, Manus Basin, Papua New Guinea. *Geochimica Et Cosmochimica Acta*, 75, 1088–1123. <https://doi.org/10.1016/j.gca.2010.11.008>
- Reeves, E. P., Yoshinaga, M. Y., Pjevac, P., Goldstein, N. I., Peplies, J., Meyerdierks, A., Amann, R., Bach, W., & Hinrichs, K. U. (2014). Microbial lipids reveal carbon assimilation patterns on hydrothermal sulfide chimneys. *Environmental Microbiology*, 16, 3515–3532. <https://doi.org/10.1111/1462-2920.12525>
- Reysenbach, A. L., John, E. S., Meneghin, J., Flores, G. E., Podar, M., Dombrowski, N., Spang, A., L'Haridon, S., Humphris, S. E., De Ronde, C. E. J., Caratori Tontini, F., Tivey, M., Stucker, V. K., Stewart,

- L. C., Diehl, A., & Bach, W. (2020). Complex subsurface hydrothermal fluid mixing at a submarine arc volcano supports distinct and highly diverse microbial communities. *Proceedings of the National Academy of Sciences of the United States of America*, 117, 32627–32638. <https://doi.org/10.1073/pnas.2019021117>
- Ryan, C. G., Kirkham, R., Hougha, R. M., Moorhead, G., Siddons, D. P., De Jonge, M. D., Paterson, D. J., De Geronimo, G., Howarde, D. L., & Cleverley, J. S. (2010). Elemental X-ray imaging using the Maia detector array: the benefits and challenges of large solid-angle. *Nuclear Instruments and Methods in Physics Research Section A*, 619, 37–43. <https://doi.org/10.1016/j.nima.2009.11.035>
- Ryan, C. G., Siddons, D. P., Kirkham, R., Dunn, P. A., Kuczewski, A., Moorhead, G., DeGeronimo, G., Paterson, D. J., De Jonge, M. D., Hough, R. M., Lintern, M. J., Howard, D. L., Kappen, P., & Cleverley, J. (2010). The new Maia detector system: methods for high definition trace element imaging of natural material. *AIP Conference Proceedings*, 1221, 9–17.
- Schauer, R., Røy, H., Augustin, N., Gennerich, H. H., Peters, M., Wenzhoefer, F., Amann, R., & Meyerdierks, A. (2011). Bacterial sulfur cycling shapes microbial communities in surface sediments of an ultramafic hydrothermal vent field. *Environmental Microbiology*, 13, 2633–2648. <https://doi.org/10.1111/j.1462-2920.2011.02530.x>
- Schieber, J., & Riciputi, L. (2005). Pyrite and marcasite coated grains in the Ordovician Winnipeg Formation, Canada: An intertwined record of surface conditions, stratigraphic condensation, Geochemical, geochemical "reworking", and microbial activity. *Journal of Sedimentary Research*, 75, 907–920.
- Schopf, W. J., Kudryavtsev, A. B., Walter, M. R., Van Kranendonk, M. J., Williford, K., Kozdon, R., Valley, J. W., Gallardo, V. A., Espinoza, C., & Flannery, D. T. (2015). Sulfur-cycling fossil bacteria from the 1.8-Ga Duck Creek Formation provide promising evidence of evolution's null hypothesis. *Proceedings of the National Academy of Sciences of the United States of America*, 112 (7), 2087–2092.
- Silhavy, T. J., Kahne, D., & Walker, S. (2010). The bacterial cell envelope. *Cold Spring Harbor Perspectives in Biology*, 2, a000414. <https://doi.org/10.1101/cshperspect.a000414>
- Skenneron, C. T., Ward, L. M., Michel, A., Metcalfe, K., Valiente, C., Mullin, S., Chan, K. Y., Gradinaru, V., & Orphan, V. J. (2015). Genomic reconstruction of an uncultured hydrothermal vent gammaproteobacterial methanotroph (family methylthermaceae) indicates multiple adaptations to oxygen limitation. *Frontiers in Microbiology*, 6, 1425. <https://doi.org/10.3389/fmicb.2015.01425>
- Takai, K., & Horikoshi, K. (1999). Genetic diversity of archaea in deep-sea hydrothermal vent environments. *Genetics*, 152, 1285–1297. <https://doi.org/10.1093/genetics/152.4.1285>
- Takai, K., Komatsu, T., Inagaki, F., & Hirokoshi, K. (2001). Distribution of archaea in a black smoker chimney structure. *Applied and Environmental Microbiology*, 67, 3618–3629. <https://doi.org/10.1128/AEM.67.8.3618-3629.2001>
- Takai, K., Nakamura, K., Toki, T., Tsunogai, U., Miyazaki, M., Miyazaki, J., Hirayama, H., Nakagawa, S., Nunoura, T., & Hirokoshi, K. (2008). Cell proliferation at 122°C and isotopically heavy CH<sub>4</sub> production by a hyperthermophilic methanogen under high-pressure cultivation. *Proceedings of the National Academy of Sciences of the United States of America*, 105, 10949–10954.
- Taylor, B. (1979). Bismarck Sea: evolution of a back-arc basin. *Geology*, 7, 171–174. [https://doi.org/10.1130/0091-7613\(1979\)7<171:BSEOA B>2.0.CO;2](https://doi.org/10.1130/0091-7613(1979)7<171:BSEOA B>2.0.CO;2)
- Thal, J., Tivey, M., Yoerger, D., Jons, N., & Bach, W. (2014). Geologic setting of PACManus hydrothermal area—high resolution mapping and in situ observations. *Marine Geology*, 355, 98–114. <https://doi.org/10.1016/j.margeo.2014.05.011>
- Thiel, J., Byrne, J. M., Kappler, A., Schink, B., & Pester, M. (2019). Pyrite formation from FeS and H<sub>2</sub>S is mediated through microbial redox activity. *Proceedings of the National Academy of Sciences of the United States of America*, 116, 6897–6902.
- Tivey, M. K. (2007). Generation of seafloor hydrothermal vent fluids and associated mineral deposits. *Oceanography*, 20, 50–65. <https://doi.org/10.5670/oceanog.2007.80>
- Van Kranendonk, M. J., Campbell, K. A., Barlow, E. V., Baumgartner, R. J., Djokic, T., Duda, G. P., & Teece, B. (2019). A pyramid of life detection for ancient life, based on deep-time Earth experience. *Astrobiology Science Conference 2019, Abs. #342-355*.
- Visscher, P. T., & Stolz, J. F. (2005). Microbial mats as bioreactors: populations, processes, and products. *Palaeogeography, Palaeoclimatology, Palaeoecology*, 219, 87–100. <https://doi.org/10.1016/j.palaeo.2004.10.016>
- Wacey, D., McLoughlin, N., Kilburn, M. R., Saunders, M., Cliff, J. B., Kong, C., Barley, M. E., & Brasier, M. D. (2013). Nanoscale analysis of pyritized microfossils reveals differential heterotrophic consumption in the ~1.9-Ga Gunflint chert. *Proceedings of the National Academy of Sciences of the United States of America*, 110, 8020–8024. <https://doi.org/10.1073/pnas.1221965110>
- Wacey, D., Saunders, M., Cliff, J., Kilburn, M. R., Kong, C., Barley, M. E., & Brasier, M. D. (2014). Geochemistry and nano-structure of a putative 3240 million-year old black smoker biota, sulphur Springs Group, Western Australia. *Precambrian Research*, 249, 1–12. <https://doi.org/10.1016/j.precamres.2014.04.016>
- Walsby, A. E. (1994). Gas vesicles. *Microbiological Reviews*, 58, 94–144. <https://doi.org/10.1128/mr.58.1.94-144.1994>
- Wang, H. L., Zyang, J., Sun, Q. L., Lian, C., & Sun, L. (2017). A comparative study revealed first insights into the diversity and metabolisms of the microbial communities in the sediments of Pacmanus and Desmos hydrothermal fields. *PLoS One*, 12(7). <https://doi.org/10.1371/journal.pone.0181048>
- Westall, F., Boni, L., & Guerzoni, E. (1995). The experimental silicification of microorganisms. *Palaeontology*, 38, 495–528.
- Westall, F., Steele, A., Toporski, J., Walsh, M., Allen, C., Guidry, S., McKay, D., Gibson, E., & Chafetz, H. (2000). Polymeric substances and biofilms as biomarkers in terrestrial materials: Implications for extraterrestrial samples. *Journal of Geophysical Research Planets*, 105, E10. <https://doi.org/10.1029/2000JE001250>
- Xie, W., Wang, F., Guo, L., Chen, Z., Sievert, S. M., Meng, J., Huang, G., Li, Y., Yan, Q., Wu, S., Wang, X., Chen, S., He, G., Xiao, X., & Xu, A. (2011). Comparative metagenomics of microbial communities inhabiting deep-sea hydrothermal vent chimneys with contrasting chemistries. *The ISME Journal*, 5, 414–426. <https://doi.org/10.1038/ismej.2010.144>
- Xu, Q., & Scott, S. D. (2005). Spherulitic pyrite in seafloor hydrothermal deposits: Products of rapid crystallization from mixing fluids. *Mineral Deposit Research: Meeting the Global Challenge*, 2005, 711–713.
- Zirenberg, R. A., Adams, M. W. W., & Arp, A. J. (2000). Life in extreme environments: Hydrothermal vents. *Proceedings of the National Academy of Sciences of the United States of America*, 97, 12961–12962. <https://doi.org/10.1073/pnas.210395997>

## SUPPORTING INFORMATION

Additional supporting information may be found in the online version of the article at the publisher's website.

**How to cite this article:** Baumgartner, R. J., Hu, S., Van Kranendonk, M. J., & Verrall, M. (2022). Taphonomy of microorganisms and microbial microtextures at sulfidic hydrothermal vents: A case study from the Roman Ruins black smokers, Eastern Manus Basin. *Geobiology*, 20, 479–497. <https://doi.org/10.1111/gbi.12490>